The Astrophysical Journal Supplement Series, 253:10 (17pp), 2021 March https://doi.org/10.3847/1538-4365/abd32d

Optical Photometry of the Quasar 3C 454.3 during the Period 2006–2018 and the Long-term Periodicity Analysis

J. H. Fan[1,2,3], S. O. Kurtanidze[4,5], Y. Liu[1,2], O. M. Kurtanidze[5,6], M. G. Nikolashvili[5], X. Liu[7], L. X. Zhang[1,2], J. T. Cai[1,2], J. T. Zhu[1,2], S. L. He[1,2], W. X. Yang[1,2], J. H. Yang[8], M. F. Gu[9], G. Y. Luo[10], and Y. H. Yuan[1,2]
[1] Center for Astrophysics, Guangzhou University, Guangzhou 510006, People's Republic of China; fjh@gzhu.edu.cn, pinux@gzhu.edu.cn
[2] Astronomy Science and Technology Research Laboratory of Department of Education of Guangdong Province, Guangzhou 510006, People's Republic of China
[3] Key Laboratory for Astronomical Observation and Technology of Guangzhou, Guangzhou 510006, People's Republic of China
[4] Samtskhe-Javakheti State University, 92 Shota Rustaveli St., Akhaltsikhe, Georgia; blazar.aao@gmail.com
[5] Abastumani Observatory, Mount Kanobili, 0301 Abastumani, Georgia
[6] Engelhardt Astronomical Observatory, Kazan Federal University, Tatarstan, Russia
[7] Xinjiang Astronomical Observatory, Chinese Academy of Sciences, Urumqi, Xijiang, People's Republic of China
[8] College of Mathematics and Physics Science, Hunan University of Arts and Science, Changde 415000, People's Republic of China
[9] Shanghai Astronomical Observatory, Chinese Academy of Sciences, Shanghai 200030 People's Republic of China
[10] School of Physics and Electronic Engineering, Guangzhou University, Guangzhou 510006, People's Republic of China
Received 2020 February 2; revised 2020 December 9; accepted 2020 December 10; published 2021 February 23

Abstract

In this work, we present 8523 pairs of *R*-band optical photometry observations for the quasar 3C 454.3 made during the period of 2006 October–2018 February on the 70 cm meniscus telescope at Abastumani Observatory, Georgia, to study its intraday variabilities (IDVs) and long-term variations, and we have come to the following results. (1) We detected 10 outbursts, a $\Delta R = 3.825$ mag variation, and some IDVs. The IDV timescales are from 4.1 to 285 minutes, with the corresponding variability amplitude being $A = 2.9\%$–43.67%. The amplitude increases with IDV timescale. (2) The largest variation over a 1 day timescale is $\Delta R = 1.38$ mag. (3) The IDV timescales suggest that the emission sizes are from 8.9×10^{13} cm to 6.20×10^{15} cm, and the magnetic field strengths are $B = 0.18$–0.79 G. (4) Period analysis results show three possible long-term periods, $p = 3.04 \pm 0.02$ yr, $p = 1.66 \pm 0.06$ yr, and $p = 1.20 \pm 0.03$ yr in the optical light curve. We adopted the accretion disk models and the lighthouse models to period $p = 3.04 \pm 0.02$ yr: in the accretion disk models, the binary black holes have masses $M = 1.17 \times 10^9 M_\odot$; in the lighthouse models, we used two boosted jet flux densities to fit the observational light curve. (5) WWZ analysis gives some short-period (high-frequency) signals associated with strong bursts (JD 2,454,302 and JD 2,454,521) with variable frequencies and lasting for the entire observation time span (11.3 yr).

Unified Astronomy Thesaurus concepts: Active galactic nuclei (16); CCD photometry (208); Quasars (1319)

Supporting material: machine-readable tables

1. Introduction

Blazars show very extreme observational properties, such as violently optical variability, high and variable polarization, superluminal motion, high energetic emissions, etc. These properties are characterized by the jet along the line of our sight (Blandford & Rees 1978; Angel & Stockman 1980; Urry & Padovani 1995; Hartman et al. 2001; Ackermann et al. 2015; Fan et al. 2016, 2017a, 2017b, 2018; Xiao et al. 2019). The spectral energy distribution of blazars is characterized by a double-bump structure, with the lower-energy bump being from a synchrotron emission and the higher-energy bump being still an open question (Fossati et al. 1998; Nieppola et al. 2006; Abdo et al. 2010; Fan et al. 2016; Lin & Fan 2018).

Variability is the typical observational property for blazars, which sheds some light on the nature and emission properties of blazars. Based on the observations, the variations have been found to have different timescales and divided into intraday variability (IDV) with the timescales, $T_{\rm Var}$ being a few minutes to 1 day, short-term variations with $T_{\rm Var}$ being a few days to months, and long-term variations (LTVs) with $T_{\rm Var}$ being years (Fan 2005). From work by Wagner & Witzel (1995), if a source shows variations of a few percent to a few tenths in the magnitude over a timescale of a day or less, then the source is said to show IDV, and this kind of variation is called IDV, microvariability, or intranight variability. The IDV is often nonperiodic, some theoretical models were proposed to explain these variations, such as the shocks propagating along the relativistic jets (Marscher & Gear 1985; Qian et al. 1991; Wagner & Witzel 1995), hot spots or disturbances on or above accretion disk surrounding the black holes (Chakrabarti & Wiita 1993; Mangalam & Wiita 1993). Although the latter mechanism is taken as the key reason for the variability in nonblazars, it can provide initial fluctuations that will be transfered into the blazar jet, resulting in Doppler boosting (Rani et al. 2010). However, the long-term variation in some cases is quasi-periodic (Jurkevich 1971; Sillanpää et al. 1988; Fan et al. 1998, 2002, 2007, 2018; Ciaramella et al. 2004; Qian et al. 2007, 2014; Ciprini et al. 2007; Valtonen et al. 2008; Rani et al. 2010; Donnarumma et al. 2011; Wiita 2011; Gupta 2014; Gaur et al. 2015; Li et al. 2015; Tavani et al. 2018).

To check the reality of a variability, we adopt a variability parameter, C, introduced by Romero et al. (1999) (see also Cellone et al. 2000), which is expressed as $C_i = \frac{\sigma_{(O-S_i)}}{\sigma_{(S_1-S_2)}}$, $i = 1$ and 2. Here $\sigma_{(O-S_i)}$ is the standard deviation of the difference of the magnitudes between the target object and a comparison star, and $\sigma_{(S_1-S_2)}$ is the deviation of two comparison stars. If $C\left(=\frac{C_1+C_2}{2}\right)$, the average value of C_1 and C_2, is greater than 2.576, then the nominal confidence level of a variability is greater than 99%.

In 1996, Heidt & Wagner introduced a variability amplitude parameter, A_m, for a variability,

$$A_m = 100 \times \sqrt{(m_{\max} - m_{\min})^2 - {\sigma_{\max}}^2 - {\sigma_{\min}}^2}\,(\%),$$

where $m_{\min}$ and $m_{\max}$ are the minimum and maximum magnitudes and $\sigma_{\min}$ and $\sigma_{\max}$ are the corresponding uncertainties.

We also introduced the following method to constrain the short-term optical variability. For any two pairs of observations $S_j(t_j, m_j)$, $S_k(t_k, m_k)$ ($j, k = 1, 2, \ldots N$), we calculated the following three parameters: time interval $\Delta t_{jk} = |t_j - t_k|$, magnitude difference $\Delta m_{jk} = |m_j - m_k|$, and the standard deviation $\sigma_{jk} = \sqrt{{\sigma_j}^2 + {\sigma_k}^2}$. If $\Delta m_{jk} > 3\sigma_{jk}$, then we take Δm_{jk} as a real variation and the corresponding time interval Δt_{jk} as the timescale. If there are more cases with $\Delta m_{jk} > 3\sigma_{jk}$, then we take the shortest Δt_{jk} as the timescales as we did in our previous works (Fan et al. 2009a, 2009b, 2014).

Later on, we tested the reality of the variation with F-test, introduced by De Diego (2010) for the reality of a variation. An F-test is a properly distributed statistics, which can be obtained by $F = \frac{S_O^2}{S_C^2}$. For two time series samples, if S_O^2 is the variance of the object's differential light-curve measurements and S_C^2 is the variance of the differential light-curve measurements of the comparison stars, then we have $F = \frac{S_O^2}{S_C^2}$.

For astronomical observations, the numbers of degrees of freedom for each sample, ν_O and ν_C, are the same and equal to $\nu = N - 1$, where N is the pair number of observations. To check the variability reality of a source, one can compare the F-value of the observations with the critical value, $F_{C(\nu_O,\nu_C)}(\alpha)$, where α is the significance level set for the test. The smaller the α, the more improbable that the result is produced by chance. A null hypothesis (no variability) is discarded if F is greater than the critical value. F-tests can be performed at two significance levels (1% and 0.1%), which correspond to 2.6σ and 3σ detections, respectively (De Diego 2010; see also Gaur et al. 2012; Xiong et al. 2017). If a variability has a high probability, then we calculate the corresponding variability amplitude A_m introduced by Heidt & Wagner (1996) and take the corresponding interval as the timescale, ΔT.

3C 454.3 (PKS 2251+158), located at $z = 0.859$ (Jackson & Browne 1991), is one of the most active blazars over the entire electromagnetic bands (Bennett 1962; Bennett et al. 2003; Worrall et al. 1987; Raiteri et al. 1998, 2007, 2008, 2011; Tavecchio et al. 2002; Fuhrmann et al. 2006; Pian et al. 2006; Villata et al. 2006, 2009; Qian et al. 2007, 2014; Giommi et al. 2006; Jorstad et al. 2010; Bachev et al. 2011; Wehrle et al. 2012; Jorstad et al. 2013; Li et al. 2015; Britto et al. 2016; Gupta et al. 2017; Kushwaha et al. 2017; Weaver et al. 2019). The historical maximum optical variation is $\Delta m = 2.3$ (Angel & Stockman 1980), and a variability of 0.5 mag over a timescale of 1 day was reported by Lloyd (1984). During our monitoring period of 2000 October carried out on the 70 cm telescope at Abstumani Observatory, Georgia, it did not show any clear variability (Fan et al. 2004). 3C 454.3 began to brighten in 2001, reaching in 2005 the brightest ever observed value in the optical band with $R = 12.0$ mag (Fuhrmann et al. 2006; Villata et al. 2006).

Periodicity analyses were investigated for 3C 454.3. Lü & Hunter (1969) reported a 340-day period; Webb et al. (1988) claimed periods of 0.83, 2.97, and 6.39 yr in its optical B band; while Su (2000) claimed a period of 12.4 yr. Ciaramella et al. (2004) found a period of about 6 yr in the radio band, The ~6 yr period was also found by Fan et al. (2007), who also claimed periods of 4.6 ± 0.1 yr, 11.8 ± 1.1 yr, and 13.6 ± 1.1 yr in its radio bands. Our recent observations show a period of ~100 minutes in its optical band (Fan et al. 2019).

Gaur et al. (2012) analyzed its observations during 2009 and 2010 and found IDVs in four nights. Based on a multiwavelength spectral model, Bonnoli et al. (2011) estimated its Doppler factors $\delta \sim 25$ during an outburst. 3C 454.3 is a potential binary black hole (e.g., Qian et al. 2007, 2014; Britzen et al. 2013). To explain the ~12.8 yr quasi-periodicity with a double-bump structure and fit the radio light curves during the period of 1966–2006, Qian et al. (2007) proposed a rotating double-jet model. Their theoretical results for the Doppler factor, δ, are from ~2.5 to ~5 for one jet and from ~10 to ~35 for another jet.

3C 454.3 is also the target in our monitoring programs at Shanghai Astronomical Observatory and Abastumani Observatory (Tao et al. 2008; Kurtanidze et al. 2009; Fan et al. 2014, 2017a) and at Xinglong Station of National Astronomical Observatories of China (NAOC) using the 1.26 m National Astronomical Observatory–Guangzhou University Infrared/Optical Telescope (NGT). In 2009 December, 3C 454.3 was detected as an extraordinary outburst at the γ-ray band by Fermi/LAT, which makes it the brightest source in the γ-ray sky (Ackermann et al. 2010; Britto et al. 2016). Weaver et al. (2019) analyzed its optical and γ-ray variabilities during its 2016 June outbursts and found that it reached maximum $S_{\rm opt} = 18.91$ mJy on 2016 June 24 and then showed a precipitous flux decay by a factor of 4 over 24 hr. A minimum timescale of 2 hr was also detected from 3C 454.3.

In the present work, we mainly search for the IDVs from our monitoring results obtained during the period of 2006 October–2018 February with the 70 cm telescope at Abstumani Observatory, Georgia. Then, we make periodicity analysis by combining the historic optical data and our own observations. This paper is arranged as follows: in Section 2, we present the observations and data reductions; in Sections 3 and 4, we show the analysis results and provide a discussion and conclusions.

2. Observations and Data Reductions

2.1. Photometry Process

Abastumani Observatory is at the top of Mount Kanobili, which is ~1700 m above sea level with a latitude of 41°.8051 and a longitude of 42°.8254. The weather and seeing conditions are good, with about 1 in 3 clear nights per year and seeing of $\leqslant 1''$. The mean values of the night-sky brightness are $B = 22.0$ mag, $V = 21.2$ mag, $R = 20.6$ mag, and $I = 19.8$ mag.

All our measurements were made on a 70 cm meniscus telescope ($f/3$), and an Apogee Ap6E CCD camera (1024×1024, 24×24 μm, quantum efficiencies are 0.40 and 0.72 at 400 and 560 nm, respectively) was attached to a primary focus. The readout, digitizing, downloading time is 1 s. We used only the central portion of 350×350 pixels^2 (15×15 arcmin^2), while the entire field of view is 40×40 arcmin^2.

2.2. Data Reductions

All the observations are obtained using the R_C passband filter (Kurtanidze & Nikolashvili 1999), and the exposure times are 60–300 s. The processing of image frames (bias correction, flat-fielding, cosmic-ray removal, etc.) and the photometry of the calibrated image frames are carried out by the standard routines

Table 1
R-band Observational Data for 3C 454.3

JD +2,454,028 (1)	m_R (mag) (2)	σ_{m_R} (mag) (3)
0.21441	15.703	0.017
0.21790	15.719	0.017
0.22140	15.683	0.017
0.23341	15.709	0.017
0.23552	15.691	0.017
0.23763	15.725	0.017
0.23973	15.733	0.017
0.24759	15.751	0.017
0.24970	15.705	0.017
0.25181	15.696	0.017

(This table is available in its entirety in machine-readable form.)

in Daophot II. For Daophot II, as we described in our previous work (Fan et al. 2014), the aperture has a fixed diameter of 10″.

First, we choose the comparison stars. For all the comparison stars, if m_i and m_j are the magnitudes of comparison stars, S_i and S_j, respectively, we calculate the differential magnitudes, Δm_{ij} ($= m_i - m_j$), and their standard deviation, $\sigma_{\Delta m_{ij}}$, of any two comparison stars in the field. Then, we choose the two stars that show the minimum deviation for all the observations as our comparison stars, S_1 and S_2.

Second, we get the magnitudes of the target object using S_1 and S_2. We first calculate the differential magnitudes $O - S_1$ and $O - S_2$ and then obtain the magnitudes, m_{S_1} and m_{S_2}, and take the average value, $m_O = \frac{1}{2}(m_{S_1} + m_{S_2})$, as the target magnitude at a time and the deviation of differential magnitude $S_1 - S_2$ of a certain night as the corresponding uncertainty for the whole observation night.

For 3C 454.3, there are nine field stars (https://www.lsw.uni-heidelberg.de/projects/extragalactic/charts/2251+158.html), for which we chose star D and star H as our comparison stars based on our observations. After the data process is adopted to our ∼11.3 yr of observations made at Abastumani Observatory, the target R magnitude and the corresponding uncertainty are obtained and listed in Table 1, in which Column (1) gives JD (+2,454,028); Column (2), R mag; and Column (3), uncertainty σ_R mag. The corresponding light curve is shown in Figure 1.

3. Results

3.1. Variation

From Figure 1, we can see 10 peaks that are located at JD 2,454,302.31 ($R = 12.348 \pm 0.012$ mag, here a Galactic extinction of $A_R = 0.286$ is adopted), JD 2,454,502.15 ($R = 13.077 \pm 0.017$ mag), JD 2,454,657.46 ($R = 13.511 \pm 0.005$ mag), JD 2,455,071.49 ($R = 14.073 \pm 0.017$ mag), JD 2,455,172.27 ($R = 13.157 \pm 0.020$ mag), JD 2,455,521.15 ($R = 12.447 \pm 0.013$ mag), JD 2,456,566.52 ($R = 14.131 \pm 0.013$ mag), JD 2,456,833.49 ($R = 13.705 \pm 0.006$ mag), JD 2,457,564.47 ($R = 12.955 \pm 0.006$ mag), and JD 2,455,324.52 ($R = 13.887 \pm 0.018$ mag). From Table 1, we can get that the magnitudes at the brightest and the faintest states are $R = 12.348 \pm 0.002$ mag at JD 2,454,302.31 and $R = 16.173 \pm 0.006$ mag at JD 2,456,090.5, corresponding to a maximum variation amplitude of $\Delta R = 3.825 \pm 0.013$ mag.

The IDV can be taken as true when a light curve obeys the following requirements: (1) the optical variabilities (Δm) are not smaller than three times σ, $\Delta M \geqslant 3 \times \sigma$ (Fan et al. 2009a, 2009b, 2014), (2) the variability parameter $C \geqslant 2.576$ (Romero et al. 2000), or (3) the F-test (De Diego 2010; see also Gaur et al. 2012).

Our observations clearly show IDVs as listed in Table 2 and Figure 2. In Table 2, Column (1) gives the observing time (JD); Column (2), magnitude at the variability occurring point (m_1); Column (3), magnitude at the variability ending point (m_2); Column (4), uncertainty of the corresponding night (σ); Column (5), pairs of observations (N). Column (6), variability index (C_1) from the difference magnitude of target and comparison star ($O - S_1$); Column (7), variability index (C_2) from the difference magnitude of target and comparison star ($O - S_2$); Column (8), F-test value (F_1) from target and comparison star ($O - S_1$); Column (9), F-test value (F_2) from target and comparison star ($O - S_2$); Column (10), critical value for the corresponding N at 99% level; Column (11), critical value for the corresponding N at 99.9% level; Column (12), variability amplitude (A%); Column (13), corresponding timescale in the units of minutes; and Column (14), variability (Y: have a variation; P: a possible variation; COM: see comments in the text).

We can see that the IDV timescales are in the range from $\Delta T = 4.1$ to 285 minutes (4.75 hr), and the corresponding variability amplitudes are in the range of $A = 2.9\%-43.67\%$.

On JD 2,454,301, it brightens from $R = 12.817$ to 12.616 mag (namely, $\Delta R = -0.201$ mag) over 98.69 minutes and then dims to $R = 12.849$ ($\Delta R = 0.233$ mag) over 130.09 minutes as shown in Figure 2(a). In each individual panel of Figure 2, there are two subpanels. The upper subpanel stands for the light curve, while the lower subpanel stands for the differential light curve of the two comparison stars plus a constant.

On JD 2,454,303, it shows a brightness decrease from $R = 12.949$ to $R = 13.386$, corresponding to a variability of $\Delta R = 0.437$ mag over 283.6 minutes; see Figure 2(b).

On JD 2,454,306, it shows a brightness decrease from $R = 13.50$ to $R = 13.733$, corresponding to a variability of $\Delta R = 0.233$ mag over 283.5 minutes as shown in Figure 2(c).

On JD 2,454,431, its brightness decreases from $R = 13.944$ to $R = 14.061$, corresponding to a variability of $\Delta R = 0.117$ mag over 36 minutes. The source also shows a flare with a fast brightness increase of 0.1 mag over 3 minutes and a fast decrease of 0.1 mag over 3 minutes; see Figure 2(d).

On JD 2,455,520, it shows a brightness increase of $\Delta R = 12.909 - 12.696 = -0.213$ (mag) over 211.7 minutes, while on JD 2,455,521, we detected a brightness decrease of $\Delta R = 12.688 - 12.437 = -0.251$ (mag) over 154.4 minutes; see Figures 2(e) and (f).

On JD 2,455,705, its brightness decreases from $R = 15.506$ to $R = 15.348$, corresponding to a variability of $\Delta R = -0.158$ (mag) over 12.9 minutes as shown in Figure 2(g).

On JD 2,457,564, its brightness increases by $\Delta R = 0.203$ mag over 13.4 minutes and then decreases. Afterward, its brightness increases by $\Delta R = 0.105$ mag over 6.2 minutes and decreases again by $\Delta R = 0.112$ mag over 13.4 minutes. See Figure 2(h).

On JD 2,457,700, its brightness increases by $\Delta R = 0.332$ mag over 285 minutes. See Figure 2(i).

On JD 2,457,994, it shows a brightness increase of $\Delta R = 0.076$ mag over 8.12 minutes; see Figure 2(j).

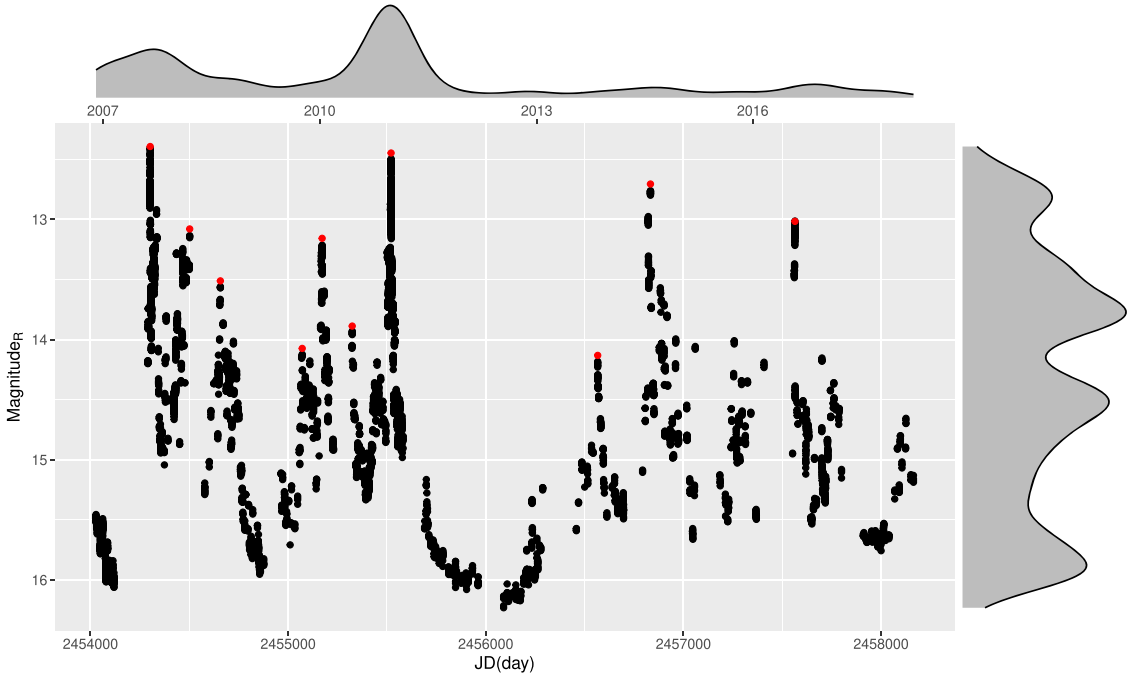

Figure 1. *R* light curve of our observations. The red dots represent the peaks of the light curve. The gray wave filled area above the figure represents the density of the time of observations, and the gray wave filled area on the right is the density distribution of the optical *R* magnitude.

Figure 1 and Table 1 indicate that, during the period from JD 2,454,060 to JD 2,454,120, the source shows a $\Delta R = 0.22$ mag brightening over 43.7 hr, shows a $\Delta R = 0.52$ mag brightening over 17 nights, and has a nearly constant brightness over 7 nights, and then it brightens from $R = 15.915$ to $R = 15.634$ ($\Delta R = -0.28$ mag) over 3 days. See Figure 3(a).

For the JD 2,454,302 peak, its brightness increases from $R = 14.139$ (JD 2,454,290.516) to $R = 12.393$ (JD 2,454,302.324) and then decreases to $R = 12.993$ (JD 2,454,308.542), and the corresponding variabilities are $\Delta R = -1.746$ mag over 12 days and $\Delta R = 1.60$ mag over 6 days as shown in Figure 3(b).

For the JD 2,454,502 peak, it consists of three peaks at JD 2,454,435 ($R = 13.231$), JD 2,454,468 ($R = 13.287$), and JD 2,454,502 ($R = 13.079$). The corresponding intervals between the two neighbor peaks are 33 days (from JD 2,454,435 to JD 2,454,468) and 34 days (from JD 2,454,468 to JD 2,454,502), respectively, as shown in Figure 3(c).

For the JD 2,454,657 peak, it brightens from $R = 15.206$ (JD 2,454,578) to $R = 13.51$ (JD 2,454,657), corresponding to $\Delta R \sim -1.7$ mag over 79 days, and then gradually dims to $R = 15.89$ (JD 2,454,856), corresponding to $\Delta R \sim 2.38$ mag over 199 days. See Figure 3(d).

For the JD 2,455,172 peak, its brightness increases from $R = 14.91$ to $R = 13.158$, corresponding to $\Delta R \sim -1.752$ mag over 15 days, and then decreases to $R = 14.863$, corresponding to $\Delta R \sim 1.705$ mag over 58 days. See Figure 3(e).

For the JD 2,455,324 peak, its brightness decreases from $R = 13.874$ to $R = 15.084$, corresponding to $\Delta R \sim 1.21$ mag over 22 days as shown in Figure 3(f).

For the JD 2,455,521 peak, it increases in brightness from $R = 14.70$ to $R = 12.487$, corresponding to $\Delta R = -2.21$ mag over 26 days, and then decreases to $R = 14.537$, corresponding to $\Delta R = 2.05$ mag over 15 days as shown in Figure 3(g).

For the JD 2,456,566 peak, its brightness increases from $R = 15.532$ to $R = 14.123$, corresponding to $\Delta R \sim -1.41$ mag over 108 days, and then decreases to $R = 15.402$, corresponding to $\Delta R \sim 1.28$ mag over 47 days. See Figure 3(h).

For the JD 2,456,833 peak, its brightness increases from $R = 14.619$ to $R = 12.705$, corresponding to $\Delta R \sim -1.91$ mag over 26 days, and then decreases to $R = 14.558$, corresponding to $\Delta R \sim 1.84$ mag over 17 days. See Figure 3(i).

For the JD 2,457,564 peak, its brightness increases from $R = 14.886$ to $R = 13.016$, corresponding to $\Delta R \sim -1.87$ mag over 12 days, and then decreases to $R = 14.393$, corresponding to $\Delta R \sim 1.38$ mag over 1 days as shown in Figure 3(j).

For the JD 2,457,701 peak, its brightness increases from $R = 15.007$ to $R = 14.094$, corresponding to $\Delta R \sim -0.91$ mag over 1 days, and then decreases to $R = 15.115$, corresponding to $\Delta R \sim 1.02$ mag over 1 days. See Figure 3(k).

Our monitoring results suggest that there are a few very rapid variabilities. On JD 2,455,577, a variation of $\Delta R = 0.184$ mag over 14.2 minutes suggests a variability ratio of 0.013 mag minute^{-1}; on JD 2,455,582, it displays a variability of $\Delta R = 0.099$ mag over 6.1 minutes, giving a ratio of 0.016 mag minute^{-1}; on JD 2,455,705, a $\Delta R = 0.158$ mag over 12.9 minutes gives 0.012 mag minute^{-1}; and on JD 2,457,620, a variability of $\Delta R = -0.017$ mag over 4.1 minutes gives 0.025 mag minute^{-1}. The ratios of the remaining IDVs are less than 0.01 mag minute^{-1}.

Our detection of $\Delta R = 0.437$ mag brightness decrease over 283.6 minutes (4.71 hr) is the largest variation over this timescale for the source. The $\Delta R = 0.91$ mag brightness increase over 1 day (JD 2,457,701) and $\Delta R = 1.38$ mag brightness decrease over 1 day (JD 2,457,564) are also the largest variations detected over a 1-day timescale. We also noticed that the source displays a nearly constant brightness over seven nights from JD 2,454,077 to JD 2,454,084

Table 2
IDV Results of FSRQ 3C 454.3

JD 2,450,000+ (1)	m_1 (2)	m_2 (3)	σ (4)	Num (5)	C_1 (6)	C_2 (7)	F_1 (8)	F_2 (9)	F^c_{99} (10)	$F^c_{99.9}$ (11)	A (%) (12)	ΔT (minutes) (13)	Var (14)
4301.3728	12.8168	12.6162	0.0083	66	7.38	7.26	63.98	60.31	1.79	2.18	20.00	98.69	Y
4301.4413	12.6162	12.8489	0.0083	67	8.01	7.70	64.21	59.31	1.79	2.17	23.27	130.95	Y
4302.3149	12.3483	12.5113	0.0118	34	4.63	4.51	21.42	20.31	2.28	3.04	16.2	50	Y
4303.3338	12.9485	13.3855	0.0100	43	15.54	15.64	241.83	244.60	2.08	2.66	43.67	283.6	Y
4306.3327	13.5000	13.7330	0.0115	100	6.31	6.28	39.93	39.63	1.60	1.88	23.27	283.50	Y
4310.3447	13.2890	13.2196	0.0073	44	3.23	2.71	10.59	7.43	2.06	2.62	6.90	251.00	Y
4431.2040	13.9440	14.0605	0.0074	11	4.59	4.15	21.04	17.25	4.85	8.76	11.57	36.70	Y
4467.2085	13.1840	13.3120	0.0145	8	3.66	3.11	13.19	9.53	6.94	14.90	13.36	16.24	P
4468.1309	13.2750	13.4950	0.0092	36	7.31	7.25	53.60	52.80	2.23	2.93	22.93	73.00	Y
4478.5266	15.2230	15.1350	0.0091	15	3.24	2.76	10.56	7.66	3.70	5.93	8.68	33.20	Y
4600.4691	14.3688	14.2960	0.0066	14	4.38	4.09	19.17	16.70	3.89	6.37	7.20	91.70	Y
5510.3418	13.3100	13.1850	0.0056	11	9.21	9.32	84.98	86.89	4.85	8.76	12.50	90.20	Y
5515.1542	13.3050	13.4240	0.0116	21	3.61	3.37	13.02	11.34	2.94	4.29	11.80	26.70	Y
5517.3478	13.3000	13.1740	0.0089	26	5.20	5.01	27.04	25.11	2.60	3.62	12.64	29.40	Y
5517.3682	13.1740	13.2596	0.0089	32	2.81	2.61	14.09	12.83	2.35	3.15	8.18	31.82	Y
5520.2113	12.9090	12.6960	0.0013	126	4.15	3.78	17.23	14.33	1.52	1.75	21.26	211.70	Y
5521.1579	12.4370	12.6880	0.0133	112	4.27	4.04	18.24	16.31	1.56	1.81	25.00	154.40	Y
5525.1573	13.5255	13.4350	0.0110	25	4.64	4.21	21.53	17.69	2.66	3.74	8.90	81.10	Y
5525.2137	13.4350	13.5879	0.0110	63	3.59	3.54	12.86	12.56	1.82	2.23	15.00	147.50	Y
5539.1363	13.8520	13.9710	0.0089	60	4.91	4.85	23.87	23.25	1.85	2.27	11.78	283.25	Y
5577.2377	14.6010	14.7630	0.0156	4	5.91	5.29	34.87	28.00	29.20	140.00	15.90	10.16	P
5577.2447	14.7630	14.5790	0.0156	6	4.54	4.92	20.67	24.23	10.90	29.40	18.20	14.20	Y
5582.2154	14.7720	14.8460	0.0048	3	6.65	7.63	44.18	58.00	99.00	999.00	7.40	4.00	P
5582.2182	14.8460	14.7469	0.0048	4	7.93	8.68	62.90	75.40	29.20	140.00	9.90	6.10	Y
5705.4929	15.5059	15.3477	0.0069	5	10.04	15.96	153.35	171.92	16.00	53.40	15.79	12.90	Y
5733.4834	15.6250	15.6490	0.0022	2	10.69	11.69	114.22	136.60	4063	20000	3.57	2.00	COM
5733.4849	15.6490	15.6087	0.0022	3	11.18	10.49	62.99	61.62	99.00	999.00	4.04	4.00	P
5901.3038	15.9065	15.9915	0.0089	5	4.88	5.50	23.85	30.26	16.00	53.40	8.37	8.10	Y
5961.0000	15.9682	15.9171	0.0069	6	3.57	4.07	12.62	16.39	10.90	29.40	5.01	10.15	P
6090.4959	16.0816	16.1732	0.0059	4	6.87	5.90	52.57	37.86	29.20	140.00	9.77	6.00	P
6090.5001	16.1732	16.0753	0.0059	3	9.85	8.90	96.98	79.30	99.00	999.00	10.34	4.00	COM
6278.2999	15.6975	15.6680	0.0019	6	5.89	6.10	31.57	33.87	10.90	29.40	2.90	15.00	Y
7564.4690	13.1581	12.9550	0.0078	12	8.36	7.97	69.94	63.63	4.43	7.70	20.20	134.00	Y
7564.4783	12.9550	13.0921	0.0078	19	6.55	6.12	42.96	37.45	3.13	4.69	13.67	21.96	Y
7564.5079	13.0889	12.9828	0.0078	6	5.15	4.64	26.51	21.47	10.90	29.40	10.56	6.20	P
7564.5122	12.9828	13.0951	0.0078	15	4.18	3.63	30.49	28.87	3.70	5.93	11.17	13.40	Y
7620.5081	14.8024	14.8195	0.0080	5	8.88	9.17	78.90	84.07	16.00	53.40	10.18	4.10	Y
7700.1708	15.0071	14.6749	0.0102	6	13.46	12.65	181.26	160.07	10.90	29.40	33.20	285.00	Y
7702.1885	14.9959	15.1152	0.0092	10	4.08	3.68	16.61	13.57	5.31	10.00	11.90	20.30	Y
7731.2616	14.9418	14.8451	0.0076	11	4.21	4.74	17.71	22.45	4.85	8.76	9.60	28.50	Y
7731.2814	14.8451	14.8946	0.0076	4	3.46	3.33	11.94	11.11	29.20	140.00	4.80	6.10	COM
7994.4330	16.062	15.986	0.005	5	6.19	5.848	65.63	54.82	16.00	53.40	7.64	8.12	Y

Note. Column (1): observing time (JD). Column (2): magnitude at the variability occurring point (m_1). Column (3): magnitude at the variability ending point (m_2). Column (4): uncertainty of the corresponding night (σ). Column (5): pairs of observations (N). Column (6): variability index (C_1) from the difference magnitude of target and comparison star ($O - S_1$). Column (7): variability index (C_2) from the difference magnitude of target and comparison star ($O - S_2$). Column (8): F-test value (F_1) from target and comparison star ($O - S_1$). Column (9): F-test value (F_2) from target and comparison star ($O - S_2$). Column (10): critical value for the corresponding N at 99% level. Column (11): critical value for the corresponding N at 99.9% level. Column (12): variability amplitude (A%). Column (13): corresponding timescale in the units of minutes. Column (14): variability (Y: have a variation; P: a possible variation; COM: see comments in the text).

(This table is available in machine-readable form.)

(Figure 3(a)), so it is possible that one cannot detect IDVs during some periods.

3.2. Period Analysis

There are some special periodic analysis methods in the literature for astronomical light curves, usually unevenly sampled time series.

Power Spectrum Analysis (PSA): The most commonly used tool for periodicity analysis of both evenly and unevenly sampled time series is the periodogram method, which is an estimator of the signal energy in the frequency domain (Deeming 1975). Lomb (1976) introduced a modified form of this method, which can be described as follows. Considering a series $x(n)$ with N points, then let f be the frequency and τ be a variable timescale. Their mean and deviation are given by

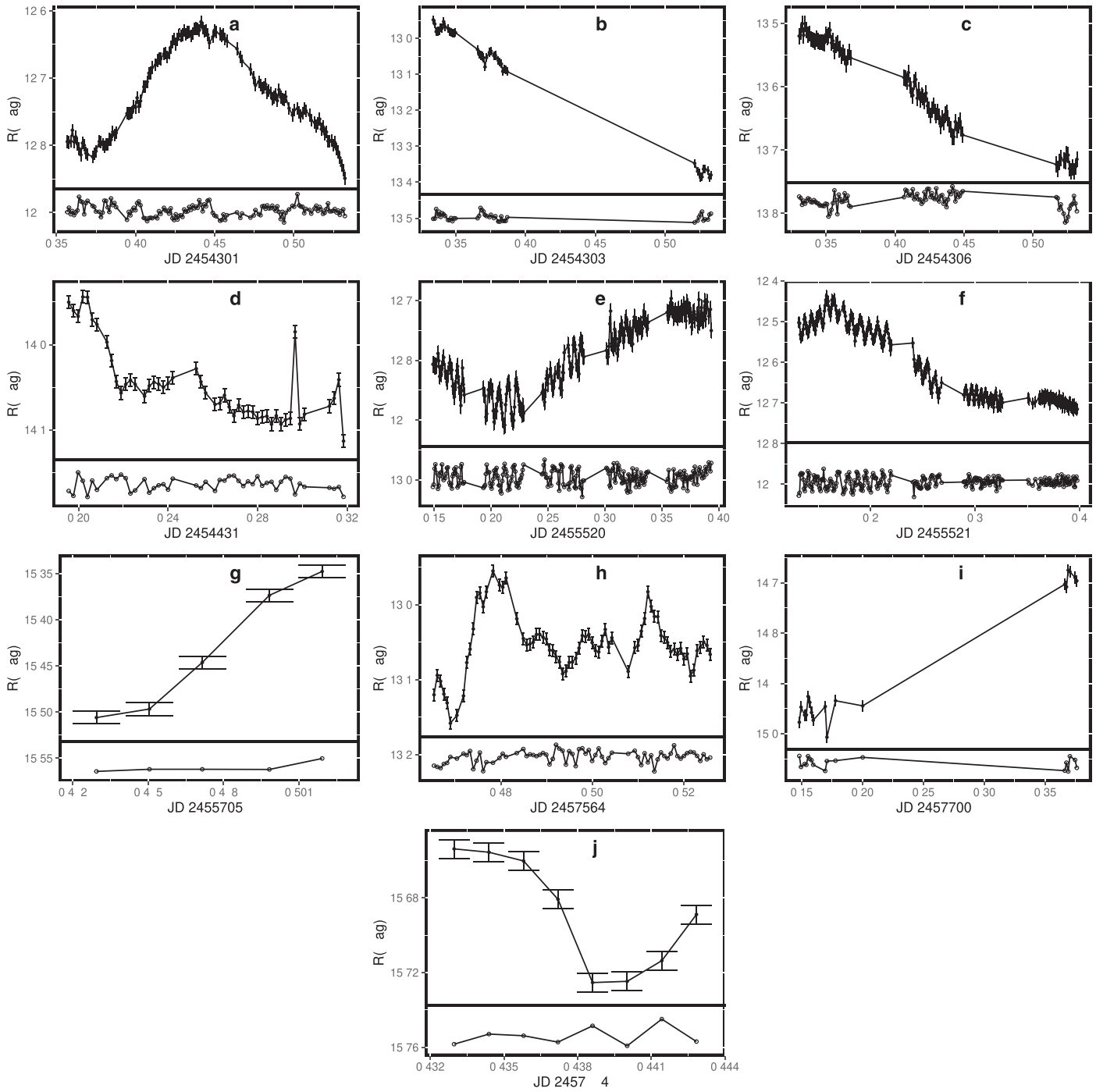

Figure 2. IDVs during our monitoring period. In each individual panel, there are two subpanels. The upper subpanel stands for the light curve, while the lower subpanel stands for the differential light curve of the two comparison stars plus a constant.

$\bar{x} = \frac{1}{N}\sum_{n=1}^{N} x(n)$ and $\sigma^2 = \frac{1}{N}\sum_{n=1}^{N}(x(n) - \bar{x})^2$. The normalized Lomb's P_N^L, i.e., the power spectrum as a function of the angular frequency $\omega \equiv 2\pi f > 0$, is defined as

$$P_N^L(\omega) = \frac{1}{2\sigma^2}\left[\frac{\left[\sum_{n=0}^{N-1}(x(n)-\bar{x})\cos\omega(t_n-\tau)\right]^2}{\sum_{n=0}^{N-1}\cos^2\omega(t_n-\tau)}\right] + \frac{1}{2\sigma^2}\left[\frac{\left[\sum_{n=0}^{N-1}(x(n)-\bar{x})\sin\omega(t_n-\tau)\right]^2}{\sum_{n=0}^{N-1}\sin^2\omega(t_n-\tau)}\right], \quad (1)$$

and τ is defined by the equation

$$\tan(2\omega\tau) = \frac{\sum_{n=0}^{N-1}\sin 2\omega t_n}{\sum_{n=0}^{N-1}\cos 2\omega t_n}. \quad (2)$$

This method can also be taken as a least-squares regression on $\sin\omega t$ and $\cos\omega t$ (Foster 1995).

The PSA technique adopted by us is the *data-compensated discrete Fourier transform*, (DCDFT) + the CLEANest algorithm (Ferraz-Mello 1981; Foster 1995). DCDFT is a

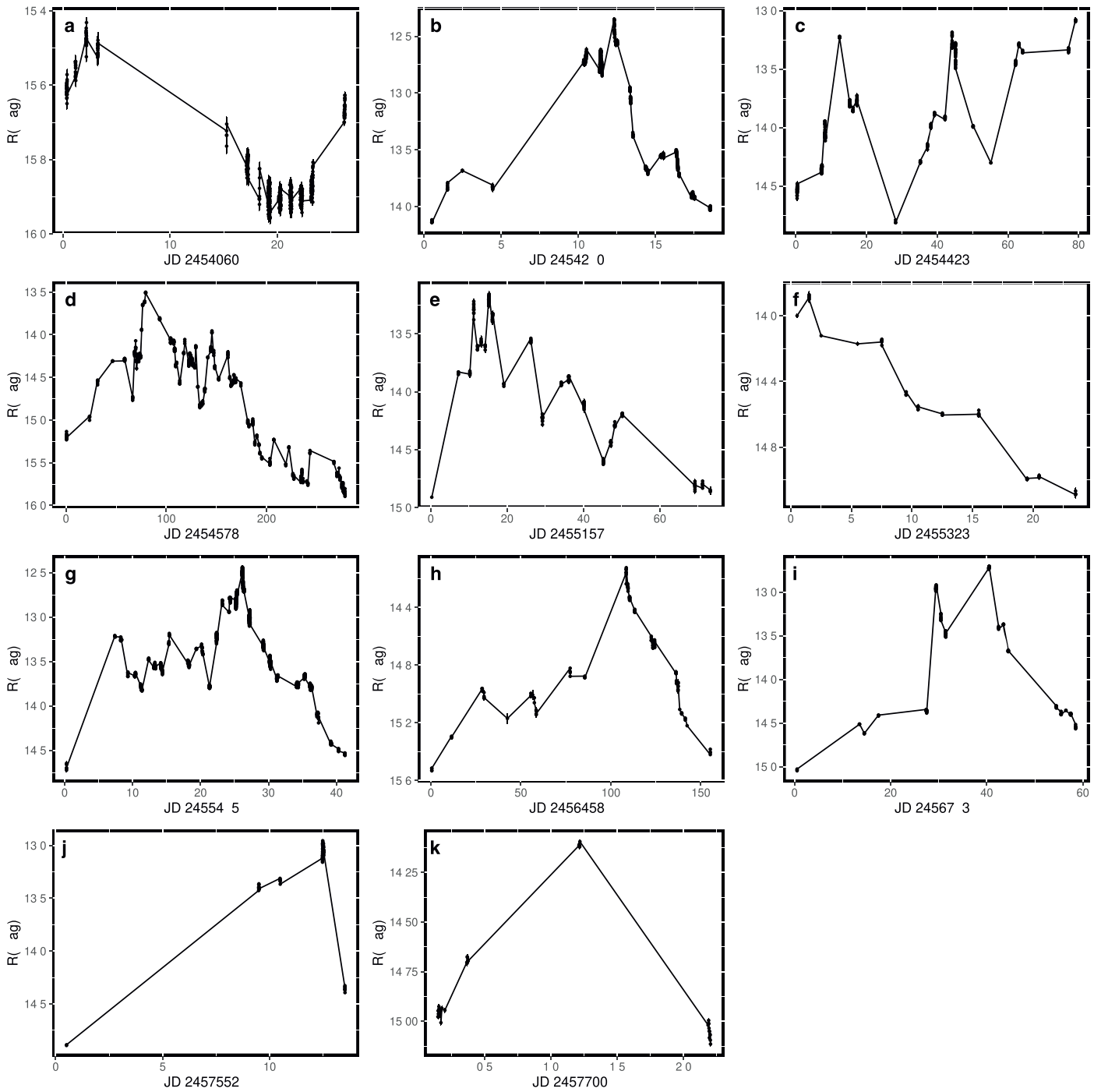

Figure 3. Optical bursts during our monitoring period.

least-squares regression on $\sin \omega t$, $\cos \omega t$, and constant. The DCDFT+CLEANest is a more powerful method than the modified periodogram for unevenly spaced data, so we used it to analyze the *R*-band light curve, following the steps described by Foster (1995).

Jurkevich Method (JV): Another method of period detection, the JV method, commonly used by astronomers, is a method basing on period folding. The JV method (Jurkevich 1971) is based on the expected mean square deviation. It tests a run of trial periods around which the data are folded. All data are assigned to m groups according to their phases around each bin, and the whole V_m^2 for each bin is computed. If the trial period is equal to the true one, then V_m^2 reaches its minimum. A "good" period will give a much reduced variance relative to those given by "false" trial periods and with almost constant values. The error in the period is estimated by calculating the HWHM of the minimum in the V_m^2.

Discrete Correlation Function (DCF): The DCF method (Edelson & Krolik 1988; Hufnagel & Bregman 1992) can explore the correlation from two variable temporal sets with a given time lag. If we only input one set, we can calculate the period of the set (Fan & Lin 2000). In order to achieve this

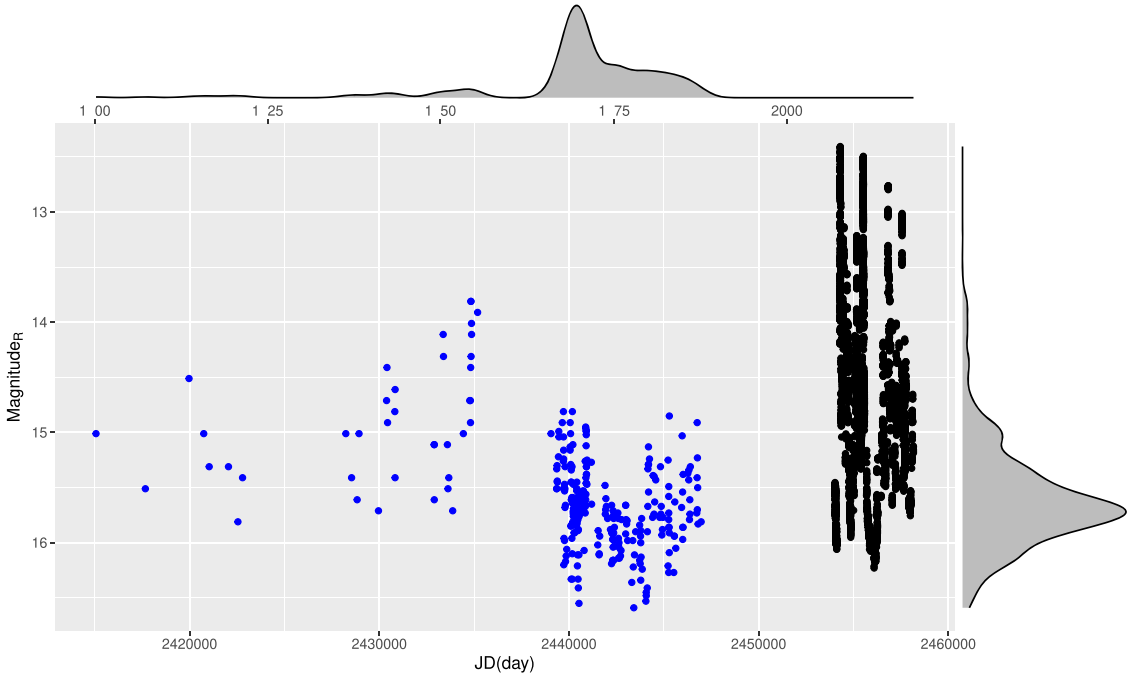

Figure 4. *R* light curves of our observations (black) and historic data (blue) from the literature. Similar to Figure 1, the gray wave filled area above the figure represents the density of the time of observations, and the gray wave filled area on the right represents the density distributions of the optical *R* magnitude.

method, first we calculate the unbinned correlation (UDCF) of the two data streams a and b, i.e.,

$$\mathrm{UDCF}_{ij} = \frac{(a_i - \langle a \rangle) \times (b_j - \langle b \rangle)}{\sqrt{\sigma_a^2 \times \sigma_b^2}}, \quad (3)$$

where a_i, b_j are two data streams, $\langle a \rangle$ and $\langle b \rangle$ being the average values of the data sets, and σ_a and σ_b being the corresponding standard deviation. Second, we average the points through sharing the same time lag by binning the UDCF_{ij} in suitably sized time bins in order to get the DCF for each time lag τ,

$$\mathrm{DCF}(\tau) = \frac{1}{M} \sum \mathrm{UDCF}_{ij}(\tau), \quad (4)$$

where M is the total number of pairs. The standard error of each bin is

$$\sigma(\tau) = \frac{1}{M} \left(\sum [\mathrm{UDCF}_{ij} - \mathrm{DCF}(\tau)]^2 \right)^{0.5}. \quad (5)$$

For 3C 454.3, our own data are shown in Figure 1. The data have 8523 pairs of observations, with a time coverage of ∼11.3 yr (4136 days) from JD 2,454,028 to JD 2,458,164. The *R* magnitude is converted into flux density using $f_R = 10^{-0.4M_R}$ mJy (Mead et al. 1990). The mean of the flux density is 8.33 ± 7.15 mJy, the minimum of f_R is 0.99 mJy, and the maximum f_R is 33.57 mJy. We adopted the subscript "*R*" to mark the parameters of the optical *R*-band data.

For 3C 454.3, historic data from the literature (Sandage 1965; Osborn 1969; Angione 1971; Tritton & Sehnes 1971; Lü 1972; Visvanathan 1973; Sehnes et al. 1975; Barbieri et al. 1978; Angione et al. 1981; Corsco et al. 1986; Sillanpää et al. 1988; Smith et al. 1988; Webb et al. 1988; Mead et al. 1990; Raiteri et al. 1998; see also Su 2000) are compiled, and then we have a time coverage of ∼118.0 yr (43,096 days) as shown in Figure 4. The density of the time of observations is plotted on the top of the figure, and the density of magnitude is plotted on the right side. The number of observations is $N = 8844$; 96.4% of the data are given by us, with an 8.6% time coverage. The beginning time is JD 2,415,068, and the ending time is JD 2,458,164. The mean flux density is 8.10 ± 7.12 mJy, the minimum f_R is 0.71 mJy, and the maximum f_R is 33.57 mJy. The subscript "*Rh*" is adopted to mark the parameters of our and the historic optical *R*-band data.

For the series of flux density over time, the DCDFT +CLEANest method is the primary detection method because it has the best performance based on our experience. For further testing, the results obtained by the CLEANest method are compared with those obtained by the JV method. Finally, based on the results obtained by DCDFT+CLEANest, a fitted time series was generated and the DCF results of it were checked for similarity with the DCF results of the real data. When the above-mentioned three methods (DCDFT+CLEANest (PSA), JV, and DCF) are adopted to the "R" and "Rh" data, we have the following results.

For the *R*-band data marked with "R," there are six CLEANest components obtained by PSA analysis, which are found as possible periodic signals. The results of the corresponding PSA period diagram (denoted with PSD_R) are plotted in the upper second panel of Figure 5, with the six CLEANest components indicated by red dots and labeled with names. Above the PSD_R plot, the JV period diagram (named with JV_R) is shown in the upper first panel of Figure 5, and it can be seen that the peaks in the PSD_R correspond to the troughs in the JV_R. The parameters of the six CLEANest components are listed in Columns (3) and (4) of Table 3, sorted by the period of the signal from longest to shortest. The first component, named P_{R2}, has a period of 2.92 ± 0.17 yr, and its relative amplitude is 2.07 ± 0.10. The second component, P_{R4}, has a period of $1.66 \pm$ yr, and its relative amplitude is 1.28 ± 0.08. The third one, P_{R1}, has a period of 1.20 ± 0.03 yr and a relative amplitude of 2.06 ± 0.10. The fourth (P_{R6}) and fifth (P_{R_5}), with periods of 0.53 ± 0.01 yr and 0.47 ± 0.01 yr,

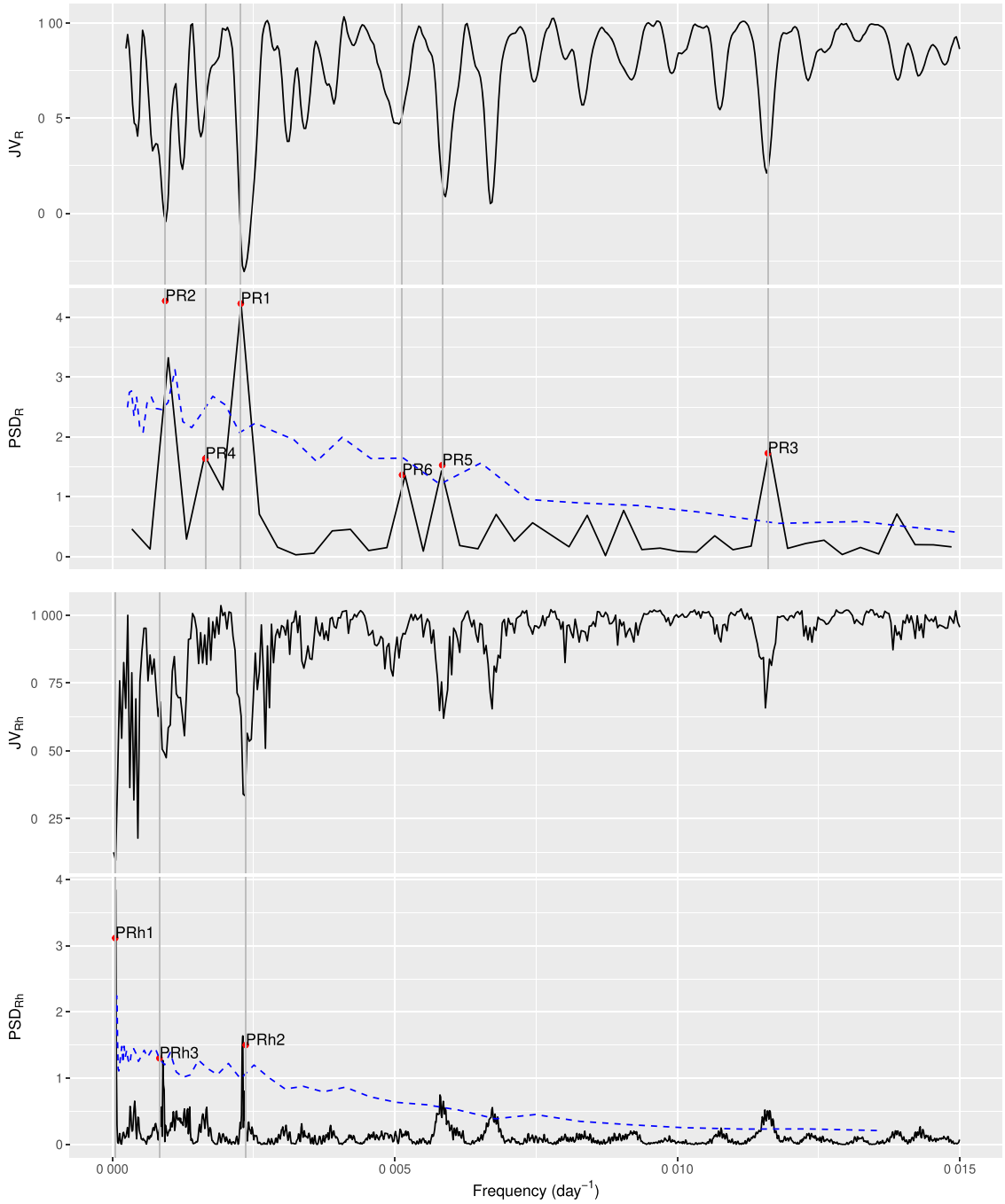

Figure 5. Period analysis results obtained by using DCDFT+CLEANest (PSD) and the JV method, for the optical data in the present work, and the combined data of the present data and the historic data, respectively. Red points labeled with names (PRi, $i = 1, 2, \cdots, 6$ and PRhi, $i = 1, 2, 3$) represent the CLEANest components. Blue dashed lines represent $1 - \mathrm{FAP} = 95\%$, which were calculated by using an ARI model of the noise.

Table 3
Period Analysis Results of Optical and Optical+Hist Data for the FSRQ 3C 454.3

Rh	T_{Rh} (yr) Time:117.5 yr	A_{Rh}	R	T_R (yr) Time:11.3 yr	A_R	$1 - \mathrm{FAP}$ (95%)
P_{Rh1}	49.63 ± 4.93	2.01 ± 0.18				$>$
P_{Rh3}	3.04 ± 0.02	1.24 ± 0.12	P_{R2}	2.92 ± 0.17	2.07 ± 0.10	$=, >, >$
			P_{R4}	1.66 ± 0.06	1.28 ± 0.08	$=$
P_{Rh2}	1.19 ± 0.03	1.22 ± 0.12	P_{R1}	1.20 ± 0.03	2.06 ± 0.10	$>, >, >$
			P_{R6}	0.53 ± 0.01	1.17 ± 0.07	$>$
			P_{R5}	0.47 ± 0.01	1.24 ± 0.07	$=$
			P_{R3}	0.24 ± 0.01	1.31 ± 0.08	$>$

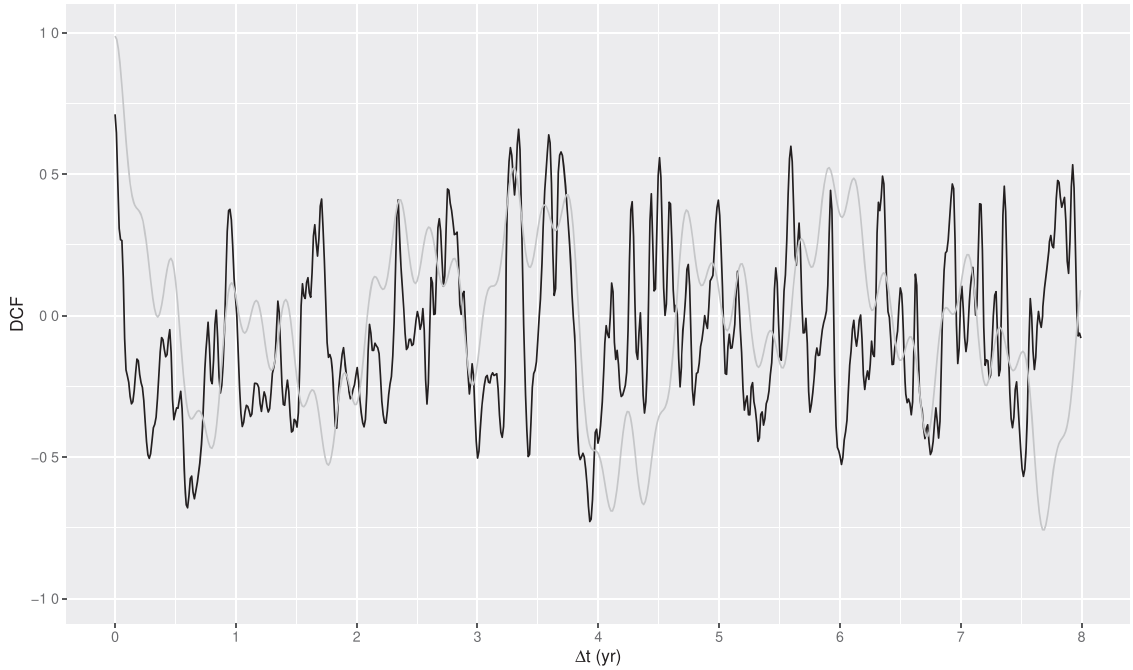

Figure 6. Period analysis results by using DCF for the optical data in the present work (black solid line). The DCF of the fitted light curve with the six CLEANest components was plotted (gray line).

respectively, have relative amplitudes of 1.17 ± 0.07 and 1.24 ± 0.07. The last one, P_{R3}, with a period of 0.24 ± 0.01 yr, has a relative amplitude of 1.31 ± 0.08.

In the R band with "Rh" data, only three CLEANest components of the possible periodic signal were found, as the historical data are very sparse and unevenly sampled (3.6% of the data occupy 91.4% of the time span, 118.0 yr). The "Rh" data are more suitable for detecting longer-period signals. The DCDFT+CLEANest period diagram PSD_{Rh} is plotted in the bottom panel of Figure 5, and the three CLEANest components are marked with red dots and labeled with the name. The Jurkevich period diagram JV_{Rh} is plotted in the panel just above the PSD_{Rh}, and troughs of JV_{Rh} and peaks of PSD_{Rh} are almost corresponding to each other. The parameters of the three CLEANest components are also listed in Columns (1) and (2) of Table 3. The first component, P_{Rh1}, has a time period of 49.63 ± 4.93 yr, almost half of the time coverage of 117.5 yr, so it is hard to be seen as a cycle. The period of P_{Rh3} is 3.04 ± 0.02 yr, which is close to the P_{R2} period of 2.92 ± 0.17 yr, and the relative amplitude is 1.24 ± 0.12. The period of P_{Rh2} is 1.19 ± 0.03 yr, which is close to the P_{R1} period of 1.20 ± 0.03 yr, and the relative amplitude is 1.22 ± 0.12.

To test the confidence of the signal, we adopted the quantity $1 - \mathrm{FAP}$ to indicate the probability that the data contain a signal, where FAP is a false-alarm probability that gives a quantitative criterion for a detection of a period signal as done in Fan et al. (2007; see also Horne & Baliunas 1986). The $1 - \mathrm{FAP}$ probability was obtained by using the Monte Carlo method from an autoregressive integrated (ARI) red noise model, and the model was produced by adopting parameters obtained based on our data. The $1 - \mathrm{FAP}$ of all six components of "R" data and three components of "Rh" data are over 95%.

Finally, the period analysis results by using DCF for the R-band data in the present work are plotted in Figure 6 (dark solid line). And the DCF of the fitted light curve with the six CLEANest components was plotted (gray line). The DCF observed and the DCF fitted correspond to each other.

3.3. Wavelet Analysis

For a given periodic signal, the intensity given by the PSA method can actually be considered as the time average of the signal intensity at each observation time t_i. These kinds of methods are very effective in detecting signals that persist and have a stable period. However, some signals may only persist for a period of time and not exist for the rest of the time, in which case the strength of the signal given by PSD decreases. There are also signals whose period may vary with time, and the intensity of the signal is spread over a wide frequency range, resulting in a significant reduction in the intensity of the single-frequency signal. All of these signals are difficult to detect using methods such as the PSA.

In order to detect periodic signals around a certain point in time, more powerful analysis methods need to be introduced. Wavelet transform analysis (Foster 1996) can decompose the time series in frequency−time space and can look for local periodicity in the data. It can detect periodic signals that exist only part of the time, such as a quasi-periodic oscillation (QPO), and can also detect signals whose period (frequency) varies with time, such as a chirp. The data of an astronomical light curve are generally unevenly sampled time series, and traditional wavelet analysis methods are difficult to use for such series. Foster (1996) proposed the weighted wavelet z-transform analysis method (WWZ), which can be used in unevenly sampled astronomical time series to search for periodic signals for the possible existence of a local area. The advantage of the wavelet method over the PSA method is that it gives the frequency and intensity of the signal over the local domain, but the disadvantage is that it reduces the resolution of the signal over the frequency domain. Sarkar et al. (2021) used WWZ to analyze light curves of 3C 454.3 in the γ band and the optical band found a 47-day QPO signal.

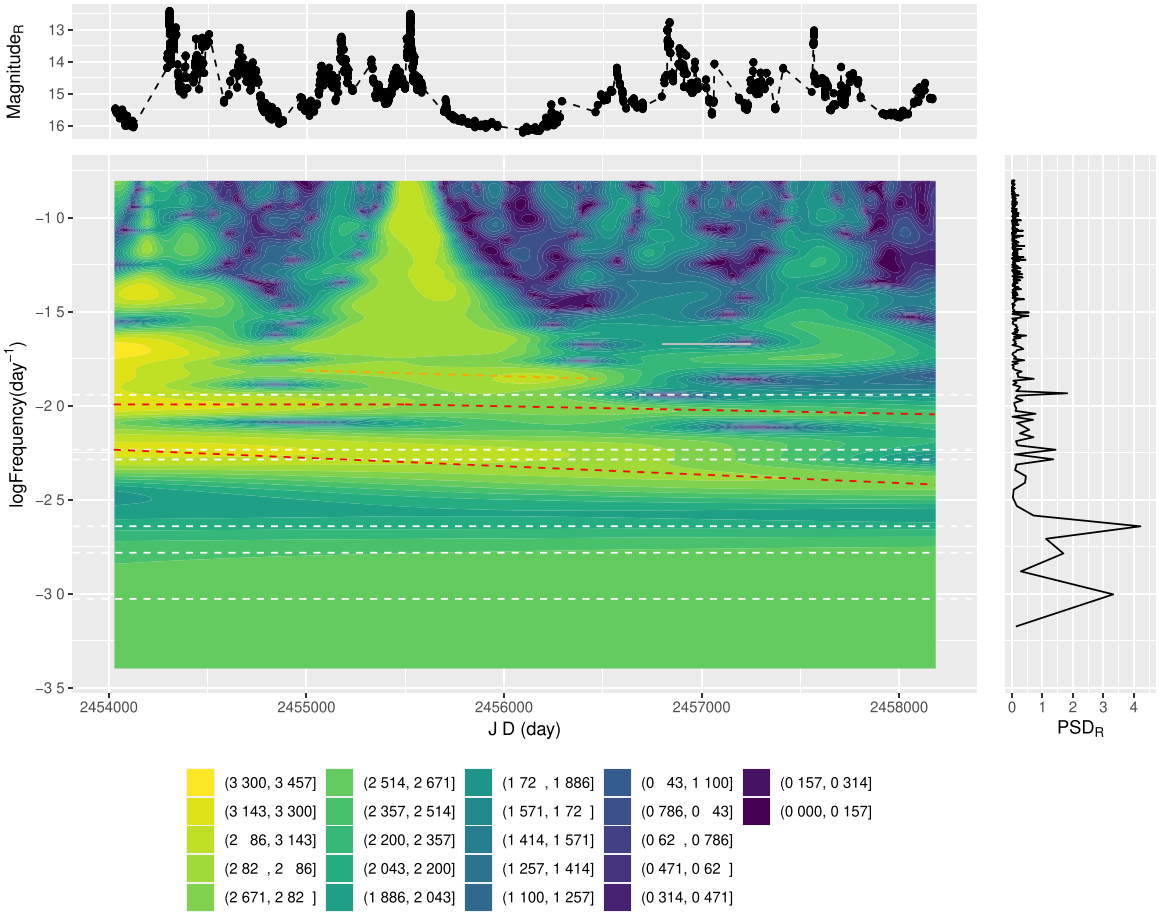

Figure 7. Main panel: wavelet analysis results by using WWZ for the *R*-band optical data in the present work. The six Cleanest components were represented by white horizontal dashed lines, with periods of 2.92, 1.66, 1.20, 0.53, 0.47, and 0.24 yr, respectively, from bottom to top. Three possible nonperiodic signals that exist in partial time are indicated by red line segments. The corresponding region of a 47-day QPO that was found by Sarkar et al. (2021) in γ-ray and optical band is marked by a gray line segments, and no corresponding signal was found, possibly because our data were sampled relatively sparsely and very unevenly in this region. Top panel: corresponding *R*-band light curve observed by us. Right panel: PSD of our light curve.

Kushwaha et al. (2020) also used WWZ for the γ-band light curve of OJ 287 and found a ∼314-day QPO.

We adopted the WWZ method (Foster 1996) to analyze our "*R*" data. The results obtained with the WWZ analysis are shown in the main panel of Figure 7, giving the color contour plot of WWZ power as a function of time and frequency. The corresponding light curves are given in the top panel of the figure, and the corresponding PSDs are given in the right panel. In the main panel of Figure 7, the six CLEANest components obtained by the PSA method are represented by white horizontal dashed lines, with periods of 2.92, 1.66, 1.20, 0.53, 0.47, and 0.24 yr, respectively, from bottom to top. Three components with longer periods (2.92, 1.66, and 1.20 yr) have greater intensities over the corresponding regions in the WWZ map but are almost fused together in the frequency domain, with periods and intensities that barely vary with time. The stronger signals given in the WWZ map have the characteristics of a chirp or QPO, as discussed in Section 4.4, and the counterparts of them can be found in the PSD, but the intensities are not very significant and the periods are shorter (0.53, 0.47, and 0.24 yr). We did not obtain an obvious signal similar to the 47-day QPO (marked by a gray line in the panel) found in the γ-ray and optical bands by Sarkar et al. (2021). This may be because our data is unevenly sampled and sparse in this period.

4. Discussion and Conclusions

Variability is a typical observation property of blazars and has been seen across all the electromagnetic wave bands (Sillanpää et al. 1988; Webb et al. 1988; Fan et al. 1998, 2002, 2007, 2014; Abraham & Caproni 2003; Caproni et al. 2004; Gu et al. 2006; Qian et al. 2007, 2014; Rani et al. 2010; Graham et al. 2015; Paliya et al. 2015; Xiong et al. 2017; Kushwaha et al. 2018; Raiteri et al. 2018; Rieger 2019; Tam et al. 2020). 3C 454.3 is one of the most variable quasars in all the electromagnetic bands (Raiteri et al. 2011; Qian et al. 2014; Gorshkov et al. 2018; Fan et al. 2019; Rajput et al. 2019; Weaver et al. 2019; Das et al. 2020) and one of the superluminal blazars (Britzen et al. 2013; Qian et al. 2014; Xiao et al. 2019). Its light curves show signs of periods 0.83 yr (Webb et al. 1988) to 12.4 yr (Su 2000) in optical bands and 1.2 yr (Gorshkov et al. 2018) to 13.6 yr (Fan et al. 2007) in the radio bands (see also Ciaramella et al. 2004; Li et al. 2006; Qian et al. 2007).

The present optical observations clearly show several optical outbursts and some IDVs. Our observations indicate a maximum amplitude variation of $\Delta R = 3.825$ mag ($R = 16.173 \pm 0.006$ to $R = 12.348 \pm 0.003$), which is larger than the historically maximum amplitude variation of $\Delta m = 2.3$ mag (Angel & Stockman 1980) and the ∼3.0 mag variation (Djorgovski et al. 2008), and is the largest variation detected in the source. In our

monitoring, we also detected the largest variations over a 1-day timescale for this source, namely, a magnitude brightness increase of $\Delta R = 0.91$ over 1 day (JD 2,457,701 Figure 3(k)) and a $\Delta R = 1.38$ mag brightness decrease over 1 day (JD 2,457,564, Figure 3(j)). Our detection of the variation over 1 day is higher than the variability of 0.5 mag by Lloyd (1984), who found that variation is over a timescale of 1 day. Our detection of 0.437 mag variation over 4.71 hr is similar to that by Lloyd (1984).

4.1. Intraday Variability

The IDVs shed some light on the emission size,

$$l \leqslant \frac{\delta c \Delta T_{\rm obs}}{1+z} = 1.08 \times 10^{14} \left(\frac{\delta}{1+z}\right)\left(\frac{\Delta T_{\rm obs}}{\rm hr}\right) {\rm cm},$$

where δ is a Doppler factor, $\Delta T_{\rm obs}$ is the IDV timescale in hours, and z is redshift.

Our monitoring results show clear IDVs as listed in Table 2. From the C-test and F-test, the high significant variabilities indicate that the variability timescales are in a range of $\Delta T = 4.1$–285 minutes. The variability amplitudes are from $A = 2.9\%$ to 43.67%. Doppler factors were estimated for 3C 454.3: $\delta_{\rm R} = 11.0$ (Padrielli 1983), $\delta_{\rm R} = 8.8$ (Huang et al. 1999), $\delta_{\rm R} = 33.2$ (Hovatta et al. 2009), $\delta_{\rm R} = 32.9$ (Savolainen et al. 2010), $\delta_{\rm R} = 26.61 \pm 2.97$ (Liodakis et al. 2018), $\delta_{\rm R} = 22.6$ (Weaver et al. 2019), $\delta_{\gamma} = 36.14$ (Zhang et al. 2020), and $\delta_{\rm R} = 11.02$ (Pei et al. 2020). When the known smallest and largest Doppler factors, $\delta = 8.8$ and 36.14, are considered, then the timescales suggest corresponding emission sizes of $l = (0.035$–$9.973) \times 10^{15}$ cm.

For a variability, we will compare the F-test values of the target and the comparison stars with the critical values for the corresponding N at 99% level (F^c_{99}) and 99.9% level ($F^c_{99.9}$). If F-test values are greater than $F^c_{99.9}$, then we take the variability to be real; if F-test values are greater than F^c_{99} but less than $F^c_{99.9}$, then we take it as a possible variability; if F-test values are less than F^c_{99}, then generally we do not take it as a variability. However, for the cases of a few pairs of observations, if the F-test values are less than F^c_{99}, but if the C-values are greater than 2.576, then we think that such a variability should be confirmed with more observations.

On JD 2,454,467, there are eight points that indicate $F^c_{99} < F_{1,2} < F^c_{99.9}$, where F_1 is the F-test value from the target and comparison star $(O - S_1)$, and F_2 is the F-test value from the target and comparison star $(O - S_2)$, so we take it as a possible IDV. Similar situations happen on JD 2,455,577, JD 2,455,961, JD 2,456,090, and JD 2,457,564. Their corresponding variability amplitudes on those 5 days are in a range of $A = 5.01\%$ to 15.90%, with their timescales being from $\Delta T = 6.0$ to 16.24 minutes as listed in Columns (12) and (13) and indicated as "P" in Column (14) of Table 2.

On JD 2,455,582, the three points give $F_{1,2} < F^c_{99}$, and the corresponding C-values are $C_1 = 6.65$ and $C_2 = 7.63$. This variability should be confirmed with more observations since we here have only three points. Similar situations appear on JD 2,455,733, JD 2,456,090, and JD 2,457,731. On JD 2,455,733, it dimmed from $R = 15.625$ to $R = 15.649$, indicating a variability of $A = 3.57\%$ over 2 minutes, and the corresponding C- and F-test values are $C_1 = 10.69$, $C_2 = 11.69$, $F_1 = 114.22$, and $F_2 = 136.6$, respectively. But there are only two sets of observations, and the critical values are $F_{99} = 4063$ and $F_{99.9} = 20000$; if this variability is true, then it is the fastest optical variability for this source.

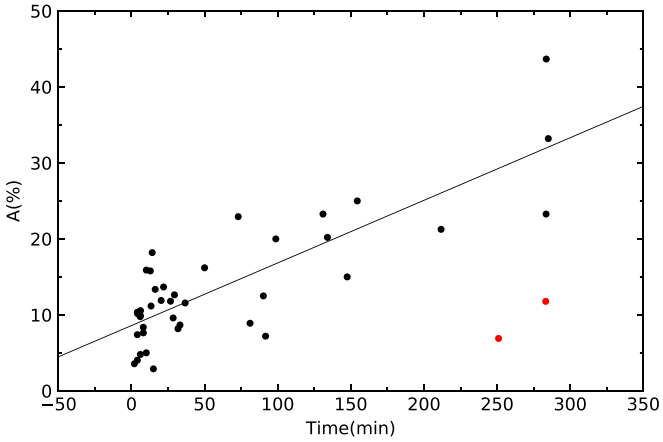

Figure 8. Plot of timescale against the variability amplitude for the IDV variability. The line stands for a best linear regression fitting result. The two points in the lower right corner are not included in the linear fitting.

On JD 2,454,431, the source shows a flare with a brightness variability of 0.1 mag over 3 minutes (Figure 2(d)). This variability is the only one case in our monitoring period, and we do not have observations in other bands, so its reality should be confirmed using more observations.

On JD 2,456,090, its brightness decreases by 9.77% over 6 minutes ($C_1 = 6.87$ and $C_2 = 5.9$, $F_1 = 52.57$ and $F_2 = 37.86$, $\Delta R = 0.092$ mag $= 15.52\sigma$) and then increases by 10.34% over 4 minutes ($C_1 = 9.85$ and $C_2 = 8.9$, $F_1 = 96.98$ and $F_2 = 79.3$, $\Delta R = -0.098 = 16.6\sigma$). Although the F-value is less than the critical F-value, the C-test and the variability amplitude ratio suggest a real variability, and the variability over 4 minutes should also be confirmed with more observations.

During the 2016 June peak, our observations show a brightness increase from $R = 14.886$ to $R = 13.016$ over 12 days, corresponding to a flux increase by a factor of 5.6 over 12 days and then a precipitous decrease to $R = 14.393$ over 1 day, corresponding to a decay by a factor of 3.6 (see Figure 3(j)). Weaver et al. (2019) found a simultaneous optical and γ-ray variability during the 2016 June outburst with a brightness slow growth and a precipitous decrease by a factor of 4 over 24 hr. The variability from our observations is consistent with that by Weaver et al. (2019).

For the available variability amplitude and the corresponding timescale, if we plot the amplitude against the timescale, we can find a tendency for the variability amplitude to increase with the IDV timescale, $A = (0.06 \pm 0.01)\Delta T + 9.33 \pm 0.95$, with a correlation coefficient $r = 0.66$ and a chance probability of $p = 2.5 \times 10^{-6}$. When the two points in the lower right corner are excluded, a better linear regression result of

$$A = (0.08 \pm 0.01)\Delta T + 8.66 \pm 0.99$$

with $r = 0.82$ and $p = 2.41 \times 10^{-10}$ can be obtained as shown in Figure 8.

For available variability timescales and the corresponding luminosity calculated from the magnitude, we plotted the logarithm of timescale against the logarithm of luminosity and found that most of the points do not obey the Elliot–Shapiro relation (1974); see Figure 9. The deviation is perhaps from the beaming effect. As mentioned above, the Doppler factors estimated for 3C 454.3 are in the range of $\delta_{\rm R} = 8.8$–36.14. When the Doppler factors, $\delta = 8.8 - 36.14$, are used to get the

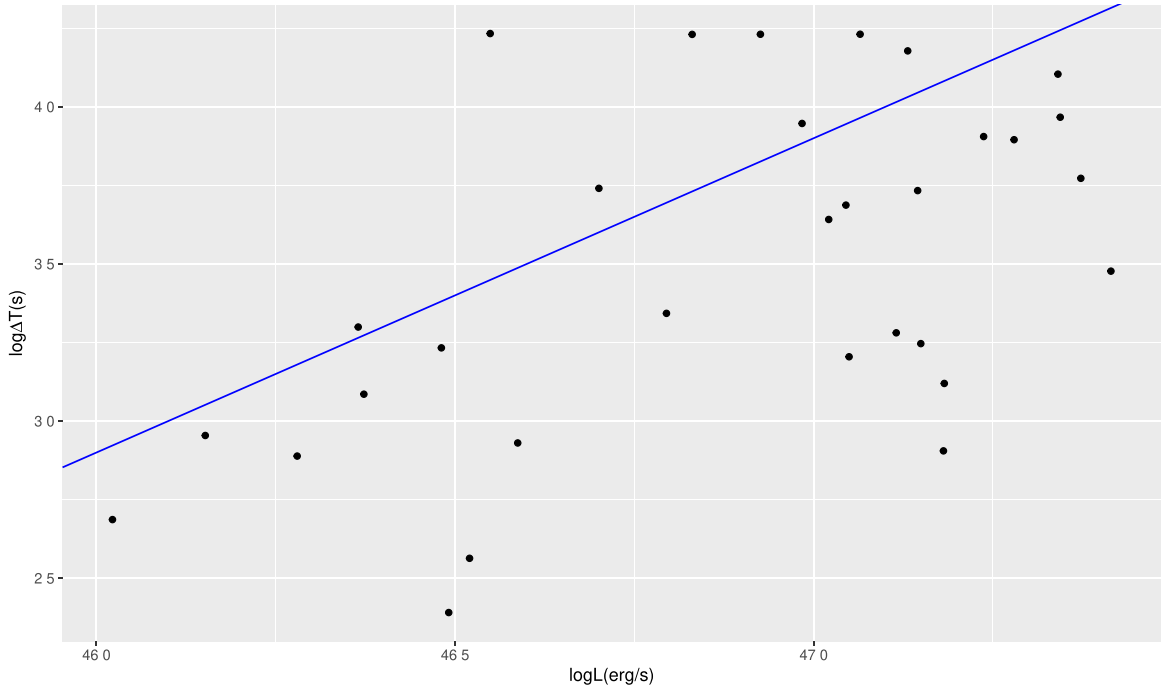

Figure 9. Plot of timescale against the optical luminosity for the IDV variability. The line stands for the Elliot–Shapiro relation.

intrinsic luminosity $L^{\rm in} = L^{\rm ob}/\delta^{4+\alpha}$ (here $\alpha = 1.0$ is adopted; Donato et al. 2001) and intrinsic timescale $\Delta t^{\rm in} = \Delta t^{\rm ob}\left(\frac{\delta}{1+z}\right)$, we found that the intrinsic data obey the Elliot–Shapiro relation, suggesting that the beaming effect is important.

4.2. Magnetic Field Strength

The intrinsic timescale of a burst was used to estimate the strength of the magnetic field in the jet. For shock-in-jet models of blazar variability (Marscher & Gear 1985), the shock energizes the relativistic electrons that enter the emitting region, and then the synchrotron and inverse Compton radiative losses will constrain the extent of the emission region. Following the work by Weaver et al. (2019), we know that in the electron energy-loss equation the total loss rate can be obtained by summing both the energy density due to the relativistic particles and the magnetic field, which are proportional to the inverse Compton and synchrotron peaks, respectively. If the ratio of the inverse Compton to the synchrotron luminosity is λ, then $u_{\rm ph} + \frac{B^2}{8\pi}$ can be rewritten as $(1+\lambda)\frac{B^2}{8\pi}$. Then, the observed lifetime ΔT (hr) of electrons emitting at a frequency ν (GHz) is associated with the magnetic field strength B (G). Thus, one can estimate the magnetic field strength B as

$$B \approx 2.35 \times 10^2 \left[\left(\frac{\delta}{10}\right)\left(\frac{1+\lambda}{1+z}\right)\left(\frac{\nu}{1\ {\rm GHz}}\right)\left(\frac{\Delta T_{\rm obs}}{1\ {\rm hr}}\right)^2\right]^{-1/3} {\rm G},$$

where z is the redshift.

As discussed above, 3C 454.3 shows IDVs with variability amplitude in R band being in the range of $A = 2.9\%$–43.67%. The timescales for the variability amplitude to be higher than 23.28% (the median value of 2.9%–43.67%) are $\Delta T = 283.6$ minutes ($A = 43.67\%$), $\Delta T = 154$ minutes ($A = 25.0\%$), and $\Delta T = 285.6$ minutes ($A = 33.20\%$); see Table 2. From Fan et al. (2016), one can find that the γ-ray and the peak synchrotron luminosities of 3C 454.3 are $\log L_\gamma = 47.49\ {\rm erg\ s^{-1}}$ and $\log L_p = 46.71\ {\rm erg\ s^{-1}}$, respectively, which implies that $\lambda = \frac{Lc}{Ls} \sim \frac{L_\gamma}{L_p} = 6.02$. This value is quite similar to the ratio of $\sim$5 of the inverse Compton (γ-ray) to synchrotron luminosity (Jorstad et al. 2013). When $\delta \sim 22.5$ and $\lambda \sim 6$ (Fan et al. 2016) are adopted, the frequency at R band is $\nu = 4.69 \times 10^5$ GHz, and then the estimated magnetic field strengths are $B = 0.53$ G for the $\sim$280-minute timescale and $B = 0.79$ G for the 154-minute timescale. If the minimum timescale of $\Delta T_{\rm obs} = 4.1$ minutes is taken into account, then $B = 11.5$ G can be obtained. When the obtained minimum and maximum values of Doppler factor, $\delta = 8.8$ and $\delta = 36.14$, are taken into account, the corresponding magnetic field strength B values are $B|_{\delta=8.8} = 1.367B|_{\delta=22.5}$ and $B|_{\delta=36.14} = 0.854B|_{\delta 22.5}$.

When we considered the peak cases with variation amplitude $\Delta R \geqslant 1.0$ mag and timescale being $\sim$1 day, there are two peaks: $\Delta R \sim 1.38$ mag over 1 day on the JD 2,457,564 peak (Figure 3(j)), and $\Delta R \sim 1.02$ mag over 1 day on the JD 2,457,701 peak (Figure 3(k)). When the above parameters ($\delta \sim 22.5$, $\lambda = 6$, $\nu = 4.69 \times 10^5$ GHz, and $\Delta T_{\rm obs} = 1$ day) are adopted, one can get $B = 0.18$ G.

Our estimation of the magnetic field strengths $B = 0.18$, 0.53, and 0.79 G is consistent with the field strength for blazars and 3C 454.3 from the literature: for blazars, $B = 0.15$ G by Zheng et al. (2019), and for 3C 454.3, $B = 0.6$ G by Hunger & Reimer (2016), $B = 0.76$ G by Chen (2018), $B = 1.0$ G by Weaver et al. (2019), and $B = 1.5$ G by Diltz & Böttcher (2016). But our estimation of magnetic field strength $B = 11.5$ G based on the 4.1 minutes is larger than those in the literature.

4.3. Periodicity

Periodical variability is common in active galactic nuclei. The long-term periodical variability with a timescale of years is perhaps from the binary black hole system (Sillanpää et al. 1988; Fan et al. 1998, 2002, 2007; Abraham & Caproni 2003; Caproni et al. 2004; Qian et al. 2007, 2014; Valtonen et al. 2008; Rieger 2019; and references therein). As a potential binary black hole, 3C 454.3 was studied for periods in its light curves. From period analyses, Webb et al. (1988) obtained three (weak) periods: 6.4, 2.97, and 0.8 yr in its optical *B* light curves during the period 1971–1985, while in the radio bands, periods of ∼6.0–6.5 yr were reported by Ciaramella et al. (2004), ∼12–13 yr by Qian et al. (2007), and from 4.6 ± 0.1 yr to 13.6 ± 1.1 yr by Fan et al. (2007).

The period of 12.8 yr in the radio bands for 3C 454.3 was explained by the lighthouse model with two jets from two black holes in a binary system (Qian et al. 2007), and the jet procession scenario was also used to explain the superluminal motions in the source (Qian et al. 2014). In blazars, the proposed precession was inferred from periodic boosting of the continuum emissions (e.g., Abraham 2000; Caproni & Abraham 2004; Caproni et al. 2004).

In the present work, the periodicity analysis methods are adopted to our own observations (*R*) and the combination of historic data and our own observations (*Rh*). We found various periods in the light curves: $p_{Rh1} = 49.63 \pm 4.93$ yr; $p_{Rh3} = 3.04 \pm 0.02$ yr and $p_{R2} = 2.92 \pm 0.17$ yr; $P_{R4} = 1.66 \pm 0.06$ yr; $p_{Rh2} = 1.19 \pm 0.03$ yr and $p_{R1} = 1.20 \pm 0.03$ yr. Hence, we can say that there are three long-term periods of $\langle p \rangle = 2.92 \pm 0.17$ yr, $\langle p \rangle = 1.66 \pm 0.06$ yr, and $\langle p \rangle = 1.20 \pm 0.03$ yr. The 49.63 yr period should be confirmed with more data in the future. There are signs of $p_{R3} = 0.24 \pm 0.01$ yr, $p_{R5} = 0.47 \pm 0.01$ yr, and $p_{R6} = 0.53 \pm 0.01$ yr in our dense monitoring. Our 0.24 yr (68 ± 4 days) period is similar to the 65-day period claimed for 3C 66A by Lainela et al. (1999) and the 47-day QPO found for 3C 454.3 by Sarkar et al. (2021). They should have the same variability mechanism, or the two sources show similar phenomena by chance.

For the JD 2,454,502 peak, it consists of three peaks, with the corresponding intervals between any two neighbor peaks being ∼33 days as shown in Figure 3(c). Does that mean that there is a period of ∼33 days during the flare state? We cannot give a definite answer since our observations are scarce for the peak. The WWZ map revealed that there are possible 50- and 25-day signals in the corresponding region near the JD 2,454,502 peak. It will be interesting to monitor the source when it is in a flare state. Therefore, our analysis indicates possible periods of 0.24, 0.47, and 0.53 yr.

However, the 12.8 yr period in radio band (Qian et al. 2007) is not observed in the present optical light curve. The reasons are perhaps from the facts that (1) the range of the optical variability amplitude is usually small and (2) the radio outbursts are usually associated with small optical flares and vice versa as discussed by Qian et al. (2007). That phenomenon is similar to the observations detected in optical and radio bands for some sources, for which when an optical burst was detected the corresponding radio band was in lower states (e.g., OJ 287, CTA 102).

For OJ 287, during its optical outburst in 1994 November the observed radio flux was very low (Pursimo et al. 2000). It is possible that the helical jets have different viewing angles with the line of sight in different bands, resulting in different boosting factors as proposed for the multiwavelength observation light curves in CTA 102 by Ratieri et al. (2018), who observed a rapid large-amplitude variation in the optical *R* band, but the variation at 37 GHz is small. Actually, the significant changes in the morphological and kinematic properties of the parsec-scale jet in 3C 454.3 were also explained geometrically because of a change in the angle to the line of sight toward the observer assuming a helical structure of the jet (Britzen et al. 2013). Therefore, for some sources, there are different periods in the optical and radio band light curves.

4.4. Nonperiodicity

As we know, for the first time, we found a signal with high WWZ power by using WWZ analysis on our *R*-band light curve of 3C 454.3, and it is obviously related to the JD 2,454,302 peak and lasted the entire time span (11.3 yr). The period of this signal is 172 ± 28 days at the beginning of our observation on JD 2,454,025, increasing to 263 ± 11 days at the final observational moment on JD 2,458,164. In the PSD analysis, the signal corresponds to the period range inside which there are two CLEANest components, signifying strong global periodic signals, $P_{R5} = 172 \pm 4$ days (0.47 yr) and $P_{R6} = 194 \pm 4$ days (0.53 yr); the PSD analysis only gives a weaker power at the period of 263 days. A signal in which the frequency is variable with time is called chirp, a signal in which the frequency increases with time is called up-chirp, and a signal in which the frequency decreases with time is called down-chirp. The logarithmic of the frequency of the signal continual linear decreases on the WWZ map, which means that the signal's property is very much like an exponential down-chirp. Meanwhile, the intensity of this signal also decreases with time.

The signal with variable frequency and intensity is defined as

$$I(t) = A(t)\sin(\phi(t)),$$

where $A(t)$ signifies the amplitude and $\phi(t)$ is the phase. Then, the frequency, f, is defined as the phase rate as given by the first derivative of phase:

$$f(t) = \frac{1}{2\pi}\frac{d\phi(t)}{dt}.$$

In an exponential chirp, the frequency $f(t)$ varies exponentially as a function of time:

$$f(t) = f_0 e^{kt},$$

where f_0 is the starting frequency (at $t = 0$) and k is the rate of exponential change in frequency. f_0 and k can be obtained by a linear fit to the logarithm of frequency and time on the WWZ map, $f_0 = 172 \pm 28$ days and $k = (-1.9 \pm 0.9) \times 10^{-5}\,\mathrm{day}^{-1}$. This signal is like a possible very low frequency down-chirp with a sustained exponential decrease in frequency over a period of about 11 yr.

The second signal with a starting frequency $\log f_0 = -1.99 \pm 0.03\,\mathrm{day}^{-1}$, which is obviously related to the JD 2,455,521 peak, has a corresponding period of 99 ± 8 days. The frequency remains almost constant from start to JD 2,455,521, followed by a small decrease to end with $\log f_0 = -2.05 \pm 0.02\,\mathrm{day}^{-1}$ (the period is 111 ± 4 days).

There is a possible third signal that starts from JD 2,455,000 and ends on JD 2,456,470 with a period 68 ± 4 days, which is also related to the JD 2,455,521 peak. And there are some

signals with much shorter periodicities that are associated with this peak.

Sarkar et al. (2021) reported that they found a simultaneous QPO in γ-ray and optical light curves of the blazar 3C 454.3, which lasted for over 450 days (from JD 2,456,800 to JD 2,457,250). There is only some very weak intensity in the frequency and time range of our data corresponding to this QPO. This should be because the resolution of our data is not dense and even enough to sample in the corresponding range of time. However, there are some ~50-day signals in the region corresponding to JD 2,454,302 peak and JD 2,455,521 peak in our WWZ map. Sarkar et al. (2021) conclude that the 47-day QPO that is most likely to originate from the scenario involves a region of enhanced emission moving helically inside a curved jet. We think that these signals may be related to shock waves in the jet.

4.5. Binary Black Hole System

As mentioned by Qian et al. (2007), the mechanisms of the optical outbursts are divided into two classes, namely, accretion models and lighthouse models. In the accretion models, the optical periodicity is caused by a precessing supermassive binary black hole system. When the secondary black hole passes through the accretion disk of the primary black hole, the accretion ratio increases to cause the optical flare, and the orbit period is the interval of the two optical flares. In this case, Doppler boosting is not being considered. However, in the lighthouse model, the periodic optical flares are proposed to be caused by the viewing angle, resulting in an increase of Doppler factor and finally resulting in an increase of observed optical flux density. The optical flares are caused purely by the Doppler boosting variation without considering the change in the accretion rate and the mass-energy transfer into the jet; see Qian et al. (2007) for details. Here, we consider both the accretion model and lighthouse model.

Accretion Model: In this model, a binary black hole model was proposed to explain such a period (Sillanpää et al. 1988; Valtonen et al. 2008). For a binary black hole system, the Kepler motion gives (Fan et al. 2014; see also Caproni & Abraham 2004)

$$p^2 = \frac{4\pi^2(a+b)^3}{G(M+m)}, \tag{6}$$

where p is the orbit period, a and b are the semiaxes, G is the gravitational constant, and M and m are the masses of the primary and the secondary black holes,

$$p \sim 1.72 M_8^{-1/2} r_{16}^{3/2}\left(1+\frac{m}{M}\right)^{-1/2} \text{yr}, \tag{7}$$

where M_8 is the mass of the primary black hole in units of $10^8 M_\odot$ and $r_{16} = a + b$ is in units of 10^{16} cm. The binary black hole system is a gravitation wave candidate, in the binary black hole system, when the r_{16} is small enough, and then the two binary black holes will merge to produce a strong gravitation wave. From observation, the period found in the light curve can be taken as the orbit period of the binary system. In this case, from the detected period in the light curve, one can estimate r_{16} when the total masses and the mass ratio are known.

For 3C 345, Caproni & Abraham (2004) proposed that the primary and the secondary black hole masses of the binary system are $4 \times 10^9 M_\odot \leqslant M_p \leqslant 5 \times 10^9 M_\odot$ and $3 \times 10^9 M_\odot \leqslant M_s \leqslant 4 \times 10^9 M_\odot$, respectively. It suggests that $M_p \sim M_s$. For 3C 454.3, if we assumed $m_8 \sim M_8$, as done by Qian et al. (2007), and adopted the averaged value of $M_8 = 11.7$ from $M_8 \sim 14.79$ (Woo & Urry 2002) and $M = 8.5 \times 10^8 M_\odot$ (Nalewajko et al. 2019), then we can get $r_{16} = 2.77$ cm.

Table 4
Parameters for the Model

Parameter	Value
Γ	20
$T_{\rm obs}$	3.04 yr
ψ_1	3°
ψ_2	10°
ϕ_1	0°
ϕ_2	105°
i	4°.70
ω	$2\pi/T_{\rm obs}$
f_{b1}	0.15×10^{-4}
f_{b2}	0.50×10^{-2}
Quiescent level	0.50 mJy

Lighthouse Model: In the work by Qian et al. (2007), they proposed to explain the periodicity in the frame of a binary black hole model with two jets from the two black holes rotating with a period of the orbital motion, and they obtained the viewing angles (θ_1 and θ_2) of the two jets to vary with time as

$$\sin\theta_1(t) = \sin\psi_1 \cos(\omega t + \phi_1)\sin i + \cos\psi_1 \cos i, \tag{8}$$

$$\sin\theta_2(t) = \sin\psi_2 \cos(\omega t + \phi_2)\sin i + \cos\psi_2 \cos i, \tag{9}$$

where ϕ_1 and ϕ_2 are azimuth angles on the orbital plane. It is assumed that at $t = 0$ the observer and component-1 are at the same azimuth angle ($\phi_1 = 0$) on the orbital plane and component-2 at ϕ_2°. Hence, one can get the Doppler factors (δ_1 and δ_2) and the flux densities (f_1 and f_2) of the two jets

$$\delta_1(t) = [\Gamma_1(1 - \beta_1 \cos\theta_1)]^{-1}, \ \delta_2(t) = [\Gamma_2(1 - \beta_2 \cos\theta_2)]^{-1}, \tag{10}$$

$$f_1(t) = f_{b1}\delta_1^4, f_2(t) = f_{b2}\delta_2^4. \tag{11}$$

When the parameters in Table 4 are adopted to $f_1(t)$ and $f_2(t)$, and we let the quiescent level be 0.5 mJy, $f(t) = f_1(t) + f_2(t) + 0.5$ is shown with a solid curve in Figure 10.

In our fitting, we adopted the lighthouse model used in the work (Qian et al. 2007, 2014). The Lorentz factor is the same as that in their work. From Figure 10, we can see that the fitting is good for most peaks.

4.6. Conclusions

In this paper, we show 8523 pairs of *R*-band photometry observations for 3C 454.3; based on the data, we discuss the IDVs and periodicity analysis and come to following conclusions:

1. During our monitoring period of 2006 October−2018 February, we detected 10 outbursts, a large-amplitude variation of $\Delta R = 3.825$ mag, and some IDVs. For those IDVs, the variability amplitudes are from $A = 2.9\%$ to 43.67% and variability timescales are from $\Delta T = 4.1$ to $\Delta T = 285$ minutes. We also found two possible

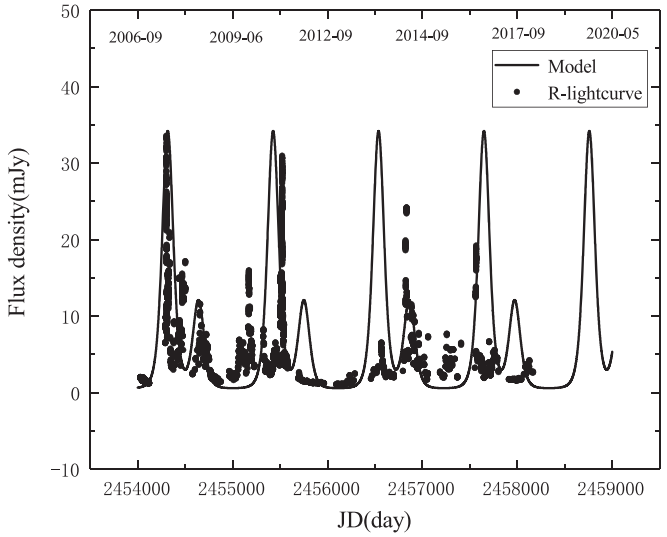

Figure 10. Observational light curve (filled points) and the theoretical light curve from the lighthouse model (solid curve) for 3C 454.3.

variabilities over 2 minutes and 3 minutes, respectively, but they should be confirmed with more observations. It is also found that the variability amplitude increases with the IDV timescale.

2. We detected the largest variation over a 1-day timescale for this source, namely, a magnitude brightness increase of $\Delta R = -0.91$ over 1 day (JD 2,457,701) and a $\Delta R = 1.38$ mag brightness decrease over 1 day (JD 2,457,564). Our result on JD 2,457,564 is consistent with that by Weaver et al. (2019).
3. From the IDV timescales, we estimated the emission size to be 8.9×10^{13} cm to 6.20×10^{15} cm. In addition, the timescales with variability amplitude higher than 23% are used to estimate the magnetic field strength (B), and $B = 0.18$–0.79 G is obtained.
4. For IDVs, the observed timescale and the corresponding luminosity do not obey the Elliot–Shapiro relation, but the intrinsic data (debeamed data) obey the relation.
5. Periodicity analyses show that there are three long-term periods: $p = 3.04 \pm 0.02$ yr, $p = 1.66 \pm 0.06$ yr, and $p = 1.19 \pm 0.03$ yr in the optical light curve. In addition, we also found some possible ∼25-, ∼33-, and ∼50-day periods, which should be confirmed with more observations. We adopted the accretion disk model and the lighthouse model to the derived period, $p = 3.04 \pm 0.02$ yr: in the accretion disk models, there is a binary black hole with the primary and the secondary black holes having the same black hole masses, $M = 1.17 \times 10^9 M_\odot$, and the semi-axis of the orbit is 2.77×10^{16} cm; in the lighthouse models, there are two jets with the Lorentz factors being $\Gamma = 20$, the azimuth angles being $\phi_1 = 0°$ and $\phi_2 = 105°$, and we used the two boosted jet flux densities to fit the observed light curve.
6. WWZ analysis gives some short-period (high-frequency) signals associated with strong bursts with variable frequencies and lasting for the entire observation time span.

We thank the anonymous reviewers for the constructive suggestions and comments. The work is partially supported by the National Natural Science Foundation of China (NSFC U1531245, NSFC U2031201, NSFC 11733001, NSFC 11873073, NSFC U2031112), Guangdong Major Project of Basic and Applied Basic Research (grant No. 2019B030302001), Natural Science Foundation of Guangdong Province (2017A030313011), supports for Astrophysics Key Subjects of Guangdong Province and Guangzhou City. The work is also supported by Guangzhou University (YM2020001, 2019GDJC-D18). S.O.K. acknowledges financial support by the Shota Rustaveli National Science Foundation under contract PHDF-18-354.

ORCID iDs

J. H. Fan https://orcid.org/0000-0002-5929-0968
S. O. Kurtanidze https://orcid.org/0000-0002-0319-5873
O. M. Kurtanidze https://orcid.org/0000-0001-5385-0576
M. G. Nikolashvili https://orcid.org/0000-0003-0408-7177

References

Abdo, A. A., Ackermann, M., Agudo, I., et al. 2010, ApJ, 716, 30
Abraham, Z. 2000, A&A, 355, 915
Abraham, Z., & Caproni, A. 2003, in ASP Conf. Ser. 299, High Energy Blazar Astronomy, ed. L. O. Takalo & E. Valtaoja (San Francisco, CA: ASP), 93
Ackermann, M., Ajello, M., Atwood, W., et al. 2015, ApJ, 810, 14A
Ackermann, M., Ajello, M., Baldini, L., et al. 2010, ApJ, 721, 1383
Angel, J. R. P., & Stockman, H. S. 1980, ARA&A, 18, 321
Angione, R. J. 1971, AJ, 76, 25
Angione, R. J., Roosen, R. G., Sievers, J., et al. 1981, AJ, 86, 653
Bachev, R., Semkov, E., Strigachev, A., et al. 2011, A&A, 528, 10
Barbieri, C., Romano, G., & Zambon, M. 1978, A&AS, 31, 401
Bennett, A. S. 1962, MmRAS, 68, 163
Bennett, C. L., Hill, R. S., Hinshaw, G., et al. 2003, ApJS, 148, 97
Blandford, R. D., & Rees, M. J. 1978, in Pittsburgh Conf. on BL Lac Objects (Pittsburgh, PA: Univ. Pittsburgh), 328
Bonnoli, G., Ghisellini, G., Foschini, L., et al. 2011, MNRAS, 410, 368
Britto, R. J., Bottacini, E., Lott, B., Razzaque, S., & Buson, S. 2016, ApJ, 830, 162
Britzen, S., Qian, S.-J., Witzel, A., et al. 2013, A&A, 557, A37
Caproni, A., & Abraham, Z. 2004, ApJ, 602, 625
Caproni, A., Cuesta, H. J. M., & Abraham, Z. 2004, ApJL, 616, L99
Cellone, S. A., Romero, G. E., & Combi, J. A. 2000, AJ, 119, 1534
Chakrabarti, S. K., & Wiita, P. J. 1993, ApJ, 411, 602
Chen, L. 2018, ApJS, 235, 39
Ciaramella, A., Bongardo, C., Aller, H. D., et al. 2004, A&A, 419, 485
Ciprini, S., Takalo, L. O., & Tosti, G. 2007, A&A, 467, 465
Corsco, G. J., Schultz, J., & Dey, A. 1986, PASP, 98, 1287
Das, A. K., Prince, R., & Gupta, N. 2020, ApJS, 248, 8
De Diego, J. A. 2010, AJ, 139, 1269
Deeming, T. J. 1975, Ap&SS, 36, 137
Diltz, C., & Böttcher, M. 2016, ApJ, 826, 54
Djorgovski, S. G., Morton, T., Drake, A. J., et al. 2008, ATel, 1684, 1
Donato, D., Ghisellini, G., Tagliaferri, G., & Fossati, G. 2001, A&A, 375, 739
Donnarumma, I., De Rosa, A., Vittorini, V., et al. 2011, ApJL, 736, L30
Edelson, R. A., & Krolik, J. H. 1988, ApJ, 333, 646
Elliot, J. L., & Shapiro, S. L. 1974, ApJL, 192, 3
Fan, J. H. 2005, ChJAS, 5, 213
Fan, J. H., Kurtanidze, O., Liu, Y., et al. 2014, ApJS, 213, 26
Fan, J. H., Kurtanidze, O., Liu, Y., et al. 2017a, ApJ, 837, 45
Fan, J. H., Kurtanidze, O., Nikolashvili, N. G., et al. 2004, ChJAA, 4, 133
Fan, J. H., & Lin, R. G. 2000, ApJ, 537, 101
Fan, J. H., Lin, R. G., Xie, G. Z., et al. 2002, A&A, 381, 1
Fan, J. H., Liu, Y., Hua, T. X., et al. 2007, A&A, 462, 547
Fan, J. H., Peng, Q. S., Tao, J., Qian, B. C., & Shen, Z. Q. 2009a, AJ, 138, 1428
Fan, J. H., Tao, J., Liu, Y., et al. 2018, AJ, 155, 90
Fan, J. H., Xie, G. Z., Pecontal, E., Pecontal, A., & Copin, Y. 1998, ApJ, 507, 173
Fan, J. H., Yang, J. H., Liu, Y., et al. 2016, ApJS, 226, 20
Fan, J. H., Yuan, Y. H., Wu, H., et al. 2019, RAA, 19, 142
Fan, J. H., Yang, J. H., & Xiao, H. B. 2017b, ApJL, 835, L38
Fan, J. H., Zhang, Y. W., Qian, B. C., et al. 2009b, ApJS, 181, 466
Ferraz-Mello, S. 1981, AJ, 86, 619
Fossati, G., Maraschi, L., Celotti, A., et al. 1998, MNRAS, 299, 433

Foster, G. 1995, AJ, 109, 1889
Foster, G. 1996, AJ, 112, 1709
Fuhrmann, L., Cucchiara, A., Marchili, N., et al. 2006, A&A, 445, 1
Gaur, H., Gupta, A. C., Bachev, R., et al. 2012, MNRAS, 425, 3002
Gaur, H., Gupta, A. C., Bachev, R., et al. 2015, A&A, 582, 103
Giommi, P., Blustin, A. J., Capalbi, M., et al. 2006, A&A, 456, 911
Gorshkov, A. G., Ipatov, A. V., Ipatova, I. A., et al. 2018, ARep, 62, 183
Graham, M. J., Djorgovski, S. G., Stern, D., et al. 2015, Natur, 518, 74
Gu, M. F., Lee, C.-U., Pak, S., Yim, H. S., & Fletcher, A. B. 2006, A&A, 450, 39
Gupta, A. C. 2014, JApA, 35, 307
Gupta, A. C., Mangalam, A., Wiita, P. J., et al. 2017, MNRAS, 472, 788
Hartman, R. C., Villata, M., Balonek, T. J., et al. 2001, ApJ, 558, 583
Heidt, J., & Wagner, S. J. 1996, A&A, 305, 42
Horne, J., & Baliunas, S. 1986, ApJ, 302, 757
Hovatta, T., Valtaoja, E., Tornikoski, M., et al. 2009, A&A, 494, 527
Huang, L. H., Jiang, D. R., & Cao, X. 1999, A&A, 341, 74
Hufnagel, B. R., & Bregman, J. N. 1992, ApJ, 386, 473
Hunger, L., & Reimer, A. 2016, A&A, 589, 96
Jackson, N., & Browne, I. W. A. 1991, MNRAS, 250, 414
Jorstad, S. G., Marscher, A. P., Larionov, V. M., et al. 2010, ApJ, 715, 362
Jorstad, S. G., Marscher, A. P., Smith, P. S., et al. 2013, ApJ, 773, 147
Jurkevich, I. 1971, Ap&SS, 13, 154
Kurtanidze, O. M., & Nikolashvili, M. G. 1999, in Proc. OJ-94 Annual Meeting, Blazar Monitoring towards the Third Millennium (Turin: Osservatorio Astronomico di Torino), 25
Kurtanidze, O. M., Tetradze, S. D., Richter, G. M., et al. 2009, in ASPC Conf. Series 408, The Starburst–AGN Connection, ed. W. Wang et al. (San Francisco, CA: ASP), 266
Kushwaha, P., Gupta, A. C., Misra, R., & Singh, K. P. 2017, MNRAS, 464, 2046
Kushwaha, P., Gupta, A. C., Wiita, P. J., et al. 2018, MNRAS, 473, 1145
Kushwaha, P., Sarkar, A., Gupta, A. C, Tripathi, A., & Wiita, P. J 2020, MNRAS, 499, 653
Lainela, M., Takalo, L. O., Sillanpää, A., et al. 1999, ApJ, 521, 561
Li, H.-Z., Xie, G.-Z., Zhou, S.-B., & Liu, H.-T. 2006, ChJAA, 6, 421
Li, H. Z., Chen, L. E., Yi, T. F., et al. 2015, PASP, 127, 1
Lin, C., & Fan, J.-H. 2018, RAA, 18, 120
Liodakis, I., Hovatta, T., Huppenkothen, D., et al. 2018, ApJ, 866, 137
Lloyd, C. 1984, MNRAS, 209, 69
Lomb, N. R. 1976, Ap&SS, 39, 447
Lü, P. K. 1972, AJ, 77, 829
Lü, P. K., & Hunter, J. H. 1969, Nat, 221, 755
Mangalam, A. V., & Wiita, P. J. 1993, ApJ, 406, 420
Marscher, A. P., & Gear, W. K. 1985, ApJ, 298, 114
Mead, A. R. G., Ballard, K. R., Brand, P. W. J. L., et al. 1990, A&AS, 83, 183
Nalewajko, K., Gupta, A. C., Liao, M., et al. 2019, A&A, 631, A4
Nieppola, E., Tornikoski, M., & Valtaoja, E. 2006, A&A, 445, 441
Osborn, W. 1969, IAU Circ., 2156
Padrielli, L. 1983, in IAU Symp. 110, VLBI and Compact Radio Sources, ed. R. Fanti et al., 169
Paliya, V. S., Böttcher, M., Diltz, C., et al. 2015, ApJ, 811, 143
Pei, Z. Y., Fan, J. H., Bastieri, D., Yang, J. H., & Xiao, H. B. 2020, SCPMA, 63, 259511
Pian, E., Foschini, L., Beckmann, V., et al. 2006, A&A, 449, L21
Pursimo, T., Takalo, L. O., Sillanpää, A., et al. 2000, A&AS, 146, 141
Qian, S.-J., Britzen, S., Witzel, A., et al. 2014, RAA, 14, 249
Qian, S. J., Kudryavtseva, N. A., Britzen, S., et al. 2007, ChJAA, 7, 364
Qian, S. J., Quirrenbach, A., Witzel, A., et al. 1991, A&A, 241, 15
Raiteri, C. M., Ghisellini, G., Villata, M., et al. 1998, A&AS, 127, 445
Raiteri, C. M., Villata, M., Acosta-Pulido, J. A., et al. 2018, Natur, 552, 374
Raiteri, C. M., Villata, M., Aller, M. F., et al. 2011, A&A, 534, 87
Raiteri, C. M., Villata, M., Chen, W. P., et al. 2008, A&A, 485, L17
Raiteri, C. M., Villata, M., Larionov, V. M., et al. 2007, A&A, 473, 819
Rajput, B., Stalin, C. S., Sahayanathan, S., Rakshit, S., & Mandal, A. K. 2019, MNRAS, 486, 1781
Rani, B., Gupta, A. C., Joshi, U. C., Ganesh, S., & Wiita, P. J. 2010, ApJ, 719, 153
Rieger, F. 2019, Galax, 7, 28
Romero, G. E., Cellone, S. A., & Combi, J. A. 1999, A&AS, 135, 477
Romero, G. E., Cellone, S. A., & Combi, J. A. 2000, A&A, 360L, 47
Sandage, A. 1965, ApJ, 146, 13
Sarkar, A., Gupta, A. C., Chitnis, V. R., et al. 2021, MNRAS, 501, 50
Savolainen, T., Homan, D. C., Hovatta, T., et al. 2010, A&A, 512, 24
Sehnes, R. A., Tritton, K. P., & Wordswork, R. W. 1975, MNRAS, 170, 15
Sillanpää, A., Haarala, S., & Korhonen, T. 1988, A&AS, 72, 347
Sillanpää, A., Haarala, S., Valtonen, M. J., Sundelius, B., & Byrd, G. G. 1988, ApJ, 325, 628
Smith, P. S., Elston, R., Berriman, G., et al. 1988, ApJL, 326, L39
Su, C. Y. 2000, AcApS, 20, 11
Tam, P. H. T., Pal, P. S., Cui, Y. D., et al. 2020, JHEAp, 26, 45
Tao, J., Fan, J., Qian, B., & Liu, Y. 2008, AJ, 135, 737T
Tavani, M., Cavaliere, A., Munar-Adrover, P., et al. 2018, ApJ, 854, 11
Tavecchio, F., Maraschi, L., Ghisellini, G., et al. 2002, ApJ, 575, 137
Tritton, K. P., & Sehnes, R. A. 1971, MNRAS, 153, 453
Urry, C. M., & Padovani, P. 1995, PASP, 107, 803
Valtonen, M., Kidger, M., Lehto, H., & Poyner, G. 2008, A&A, 477, 407
Villata, M., Raiteri, C. M., & Balonek, T. J. 2006, A&A, 453, 817
Villata, M., Raiteri, C. M., Gurwell, M. A., et al. 2009, A&A, 504, L9
Visvanathan, N. 1973, ApJ, 179, 1
Wagner, S. J., & Witzel, A. 1995, ARA&A, 33, 163
Weaver, Z. R., Balonek, T. J., Jorstad, S. G., et al. 2019, ApJ, 875, 15
Webb, J. R., Smith, A. G., Leacock, R. J., et al. 1988, AJ, 95, 374
Wehrle, A. E., Marscher, A. P., Jorstad, S. G., et al. 2012, ApJ, 758, 72
Wiita, P. J 2011, JApA, 32, 147
Woo, J. H., & Urry, C. M. 2002, ApJ, 579, 530
Worrall, D. M., Tananbaum, H., Giommi, P., & Zamorani, G. 1987, ApJ, 313, 596
Xiao, H. B., Fan, J. H., Yang, J. H., et al. 2019, SCPMA, 62, 129811
Xiong, D., Bai, J. M., Zhang, H. J., et al. 2017, ApJS, 229, 21
Zhang, L. X., Chen, S. N., Xiao, H. B., Zhu, J. T., & Fan, J. H. 2020, ApJ, 897, 10
Zheng, Y. G., Kang, S. J., Yang, C. Y., & Bai, J. M. 2019, ApJ, 873, 7

The Astrophysical Journal Supplement Series, 260:22 (1pp), 2022 May https://doi.org/10.3847/1538-4365/ac6ba7

Erratum: "Optical Photometry of the Quasar 3C 454.3 during the Period 2006–2018 and the Long-term Periodicity Analysis" (2021, ApJS, 253, 10)

J. H. Fan[1,2,3], S. O. Kurtanidze[4,5], Y. Liu[1,2], O. M. Kurtanidze[5,6], M. G. Nikolashvili[5], X. Liu[7], L. X. Zhang[1,2], J. T. Cai[1,2], J. T. Zhu[1,2], S. L. He[1,2], W. X. Yang[1,2], J. H. Yang[8], M. F. Gu[9], G. Y. Luo[10], and Y. H. Yuan[1,2]
[1] Center for Astrophysics, Guangzhou University, Guangzhou 510006, People's Republic of China; fjh@gzhu.edu.cn, blazar.aao@gmail.com, pinux@gzhu.edu.cn
[2] Astronomy Science and Technology Research Laboratory of Department of Education of Guangdong Province, Guangzhou 510006, People's Republic of China
[3] Key Laboratory for Astronomical Observation and Technology of Guangzhou, Guangzhou 510006, People's Republic of China
[4] Samtskhe-Javakheti State University, 92 Shota Rustaveli St., Akhaltsikhe, Georgia
[5] Abastumani Observatory, Mount Kanobili, 0301 Abastumani, Georgia
[6] Engelhardt Astronomical Observatory, Kazan Federal University, Tatarstan, Russia
[7] Xinjiang Astronomical Observatory, Chinese Academy of Sciences, Urumqi, Xinjiang, People's Republic of China
[8] College of Mathematics and Physics Science, Hunan University of Arts and Science, Changde 415000, People's Republic of China
[9] Shanghai Astronomical Observatory, Chinese Academy of Sciences, Shanghai 200030, People's Republic of China
[10] School of Physics and Electronic Engineering, Guangzhou University, Guangzhou 510006, People's Republic of China
Received 2022 April 28; published 2022 May 13

In the published article, due to our typing mistake, Equations (8) and (9) were incorrect. We wish to correct the definition as follows:

$$\cos\theta_1(t) = \sin\psi_1\cos(\omega t + \phi_1)\sin i + \cos\psi_1\cos i, \tag{8}$$

$$\cos\theta_2(t) = \sin\psi_2\cos(\omega t + \phi_2)\sin i + \cos\psi_2\cos i \tag{9}$$

where θ_1 and θ_2 are the viewing angles of the two jets. Equations (8) and (9) here are identical to the expressions in Equations (1) and (2) in Qian et al. (2007).

This correction does not have any effect on our final results, since this error only occurred during typing. Both equations used in our corresponding calculations are correct.

ORCID iDs

J. H. Fan https://orcid.org/0000-0002-5929-0968
J. T. Cai https://orcid.org/0000-0002-8960-1544
J. T. Zhu https://orcid.org/0000-0002-8206-5080

References

Qian, S.-J., Kudryavtseva, N. A., Britzen, S., et al. 2007, ChJA&A, 7, 364